UNIVERSIDADE FEDERAL DE MINAS GERAIS
PROGRAMA DE PÓS-GRADUAÇÃO EM SANEAMENTO,
MEIO AMBIENTE E RECURSOS HÍDRICOS

NUMERICAL MODELING OF A 90° OPEN-CHANNEL CONFLUENCE FLOW USING OPENFOAM CFD

Victor Manoel Pavanelli Lira

Belo Horizonte
2014

NUMERICAL MODELING OF A 90° OPEN-CHANNEL CONFLUENCE FLOW USING OPENFOAM CFD

Victor Manoel Pavanelli Lira

Victor Manoel Pavanelli Lira

NUMERICAL MODELING OF A 90° OPEN-CHANNEL CONFLUENCE FLOW USING OPENFOAM CFD

Dissertação apresentada ao Programa de Pós-graduação em Saneamento, Meio Ambiente e Recursos Hídricos da Universidade Federal de Minas Gerais, como requisito parcial à obtenção do título de Mestre em Saneamento, Meio Ambiente e Recursos Hídricos.

Área de concentração: Recursos Hídricos

Linha de pesquisa: Modelagem Física e Matemática em Hidráulica

Orientador: Luiz Rafael Palmier

Belo Horizonte
Escola de Engenharia da UFMG
2014

Lira, Victor Manoel Pavanelli.
L768n Numerical modeling of a 90° open-channel confluence flow using OpenFOAM CFD [manuscrito] / Victor Manoel Pavanelli Lira.- 2014.
xi, 71 f.: il.

Orientador: Luiz Rafael Palmier.

Dissertação (mestrado) – Universidade Federal de Minas Gerais, Escola de Engenharia.

Bibliografia: f. 69-71.

1. Engenharia sanitária - Teses. 2. Recursos hídricos - Desenvolvimento - Teses. I. Palmier, Luiz Rafael. II. Universidade Federal de Minas Gerais, Escola de Engenharia. III. Título.

CDU: 628(043)

ACKNOWLEDGEMENTS

After this long joint Master's course, my gratitude is given to relatives, friends, colleagues and professors, lovely people from different countries and two high quality universities.

First and foremost I must thank all employees and brilliant professors from my home university, Federal University of Minas Gerais, for offering this inspiring Master's programme, and particularly to my supervisor prof. dr. ir. Luiz Rafael Palmier for pushing me forward and enhancing the quality and value of my research.

Secondly, I have to thank my research supervisor at Ghent University prof. dr. ir. Tom De Mulder, for believing in me, proposing such a challenging and enriching research theme, and providing the resources I needed to develop this work. My gratitude to all colleagues of the Hydraulics Laboratory, a welcoming and pleasant working environment, specially ir. Laurent Schindfessel and ir. Stéphan Creelle who provided me with important insights, material and dedication. The computational resources (Stevin Supercomputer Infrastructure) and services used in this work were provided by the VSC (Flemish Supercomputer Center), funded by Ghent University, the Hercules Foundation and the Flemish Government – department EWI.

I would not have gotten this far, literally, without the financial support of BABEL project (Erasmus Mundus Programme), coordinated by the University of Porto. So here is my appreciation to all these institutions and personnel for investing in my future.

I cannot forget my colleagues from Leme Engenharia, my former boss dr. ir. Ricardo Junho and all who instructed and inspired me to become a great professional.

It was a wonderful period in both Belo Horizonte and Ghent. Many enduring friendships were made from companies, universities, church, judo clubs, and everywhere. My gratitude to all of them for becoming part of my life and making this experience truly significant.

Thanks to my parents and family, for supporting me with words and deeds. The most special thanks to Fernanda, the woman of my life, my best friend and supporter, who is always willing to sacrifice her life for the sake of my dreams and ours as a team. Finally, my eternal gratitude to God for bringing me to this amazing country and for guiding me again through all challenges. His love, hope and joy were my strength.

ABSTRACT

Numerical modeling of flows is an important tool used before building proper physical models of hydraulic structures. In some projects, when the construction of physical models is not economically feasible, numerical models are used to directly evaluate the performance of these structures and to determine final details in their design. A large variety of numerical methods and turbulence models has been developed in the last three decades seeking to represent the enormous range of types of flows existing in nature or in industry. Although, there is still a gap between the foretold potential of this models and the assurance of their accuracy for different cases.

Accordingly, the aims of this study are to set up a three-dimensional numerical model and to evaluate the accuracy of different turbulence models of reproducing the flow characteristics of a 90º open channel confluence, which, though consisting of a common and simple geometry, produces a roundly three-dimensional flow, not easy to be reproduced in numerical models.

OpenFOAM, a free and open source CFD software, was used in this research. The experimental data used for validating the numerical models was taken from the experiments made by Weber et al. (2001). The most three dimensional flow scenario was analyzed, when q^* = main channel inflow / total outflow = 0,25. Velocity fields were compared to evaluate the accuracy of simulation results from three different turbulence models [the Re-Normalization Group (RNG) k-ε model, the k-ω model and a Large Eddy Simulation (LES) model]. The water-surface was treated by a rigid lid approach.

The general flow behavior generated by the numerical models was in good agreement with the experimental results, regardless of the rigid lid approach's natural inability of modeling the free-surface. However none of the turbulence models could reproduce properly the secondary current or the helicoidal current downstream the junction. Though the LES model was meant to be more powerful, its accuracy was worse than the two-equation turbulence models'. No big difference was found in the performance of the RNG k-ε and the k-ω models. However, since the RNG k-ε better predicted the separation zone, it can be said that it was the most efficient turbulence model for the case analyzed in this research.

RESUMO

Modelagem numérica de escoamentos é uma importante ferramenta utilizada antes de construir modelos físicos adequados de estruturas hidráulicas. Em alguns projetos, quando a construção de modelos físicos não é economicamente viável, modelos numéricos são utilizados para avaliar diretamente o desempenho dessas estruturas e para determinar os detalhes no projeto executivo. Uma grande variedade de métodos numéricos e modelos de turbulência tem sido desenvolvida nas últimas três décadas pretendendo representar a enorme variedade de tipos de fluxo existentes na natureza ou na indústria. Entretanto, ainda há uma lacuna entre o potencial desses modelos e a garantia da sua precisão para casos distintos.

Assim, os objetivos deste estudo são: montar um modelo numérico tridimensional e avaliar a precisão dos diferentes modelos de turbulência ao reproduzir as características do escoamento livre em uma confluência 90° que, embora constituída por uma geometria comum e simples, produz um fluxo tridimensional e helicoidal que não é fácil de ser modelado.

O OpenFOAM, um software de código CFD livre e aberto, foi utilizado. Os dados experimentais utilizados para validação foram obtidos de Weber *et al.* (2001). Foi analisado o cenário de escoamento de maior característica tridimensional, no qual q* = vazão de entrada no canal principal / vazão de saída = 0,25. Campos de velocidade foram comparados para avaliar a precisão dos resultados de simulação a partir de três diferentes modelos de turbulência [o modelo *Re-Normalization Group* (RNG) k-ε, o modelo k-ω e um modelo *Large Eddy Simulation* (LES)]. A superfície da água foi tratada como uma tampa rígida e sem atrito.

O comportamento geral do fluxo gerado pelos modelos numéricos é de boa concordância com os resultados experimentais, independentemente da incapacidade natural da abordagem da tampa rígida em modelar a superfície da água. No entanto, nenhum dos modelos de turbulência pôde reproduzir precisamente a corrente secundária ou a corrente helicoidal a jusante da junção. Embora o modelo LES tenha sido concebido para ser mais eficaz, sua precisão foi pior do que a dos modelos de turbulência de duas equações. Não foi encontrada grande diferença entre o desempenho dos modelos RNG k-ε e k-ω. No entanto, uma vez que o RNG k-ε melhor representou a zona de separação, pode-se dizer que foi o modelo de turbulência mais eficaz para o caso analisado nesta pesquisa.

TABLE OF CONTENTS

LIST OF FIGURES

LIST OF TABLES

TABLES OF ABBREVIATION AND SYMBOLS

Abbreviation	Meaning
1D, 2D or 3D	One, Two or Three dimensional
BFC	Body-Fitted Coordinate grid
CAR	Cartesian grid
CFD	Computational Fluid Dynamics
HOL	Height Of Liquid concept
LES	Large Eddy Simulation
POR	Porosity concept
RANS	Reynolds-Averaged Navier-Stokes
RL	Rigid Lid assumption
RNG	Re-Normalization Group
RSM	Reynolds Stress Model
VOF	Volume Of Fluids method

Symbol	Name	Unity
$\bar{u}$, $\bar{v}$ and $\bar{w}$	Filtered velocities in the x-, y- and z-direction	m/s
$\bar{\mathbf{u}}$	Filtered velocity vector	m/s
μ	Dynamic viscosity	Pa.s
A_c	Cross-sectional area of the computational flume	m^2
F_r	Froude number	-
H_o	Tailwater depth	m
I	Turbulence intensity	%
K	Mean kinetic energy	$kg.m^2/s^2$
k	Turbulent kinetic energy	$kg.m^2/s^2$
k(t)	Instantaneous kinetic energy	$kg.m^2/s^2$
k_p	Turbulent kinetic energy at the patch	m^2/s^2
ℓ	Large-eddy length scale	M
p	Pressure	Pa
q*	Flow ratio (Q_m / Q_t)	-
Q_b	Branch channel inflow	m^3/s
Q_m	Main channel inflow	m^3/s
Q_t	Outflow	m^3/s
s_{ij}	Linear deformation rate components	-
t	Time	s
U	Steady mean velocity vector	m/s
u	Velocity vector	m/s
U, V and W	Steady mean scalar velocities in the x-, y- and z-direction	m/s
u,v and w	Scalar velocities in the x-, y- and z-direction	m/s
u’	Fluctuating velocity vector	m/s
u’, v’ and w’	Fluctuating scalar velocities in the x-, y- and z-direction	m/s
U_t	Outlet average velocity	m/s
W	Channel width	m
x, y and z	Coordinates	m
y^+	Dimensionless distance to the wall	-
ε	Rate of dissipation of k per unit mass	m^2/s^3
ϑ	Large-eddy velocity scale	m/s

λ	Volumetric deformation viscosity	Pa.s
ν	Kinematic viscosity	m^2/s
ρ	Density	kg/m^3
τ_{ij}	Viscous stresses component	s^{-1}
ω	Turbulence frequency	s^{-1}

1 INTRODUCTION

1.1 Overview

The desire of understanding and predicting natural phenomena is apparently intrinsic in human nature. Since ancient times people work on observing nature and elaborating scientific models of some of its features. A scientific model has the aim to make a particular part or feature of the world easier to understand, define, quantify, visualize, or simulate. When it comes to designing hydraulic structures, predicting flow features is not only a desire, but a requirement.

In hydraulic engineering, as in other fields, structures can be designed by applying four different modeling resources: simple calculations based on analytical (theoretical) equations; calculations based on empirical (experimental) equations; numerical models; and small scale physical models. The first two categories are usually used to make the conceptual design providing the necessary dimensions of a structure, while the two last are applied when a better understanding of the flow patterns is necessary to properly design the details of a structure and its protection.

A numerical model employs numerical methods and algorithms to solve mathematical equations that aim to reproduce a physical phenomenon into a geometry, given certain boundary and initial conditions. Thanks to the technological development of computational resources, the numerical models, some developed several decades ago, could recently start being applied by industry and common users to simulate complex fluid flows. As a result, numerical models became an important tool used before building proper physical models in order to reduce the overall project cost. In some smaller projects, when the construction of physical models is not economically feasible, numerical models are used to directly evaluate the performance of hydraulic structures and to determine final details in their design.

A large variety of numerical methods and turbulence models has been developed seeking to represent the enormous range of types of flows existing in nature and in industry. Nevertheless, there is still a gap between the foretold potential of this models and the assurance of their accuracy for different cases. Therefore, the more study cases available in literature, the more secure users may get when choosing the settings.

It is important to mention that successful modeling is not guaranteed by the usage of powerful softwares. It is rather better pursued by seeking to understand the physical phenomena, i.e. expected flow patterns, as well as the numerical model, i.e. governing equations and numerical methods. In fact, a computational model, robust or not, in the hands of an inexperienced user has the potential to do great harm. This project was born, therefore, from the desired of the author to gain experience in the theme and to get acquainted to its difficulties and limitations.

The study case modeled was a 90° open-channel confluence. The reasons for such a choice are: a confluence is a very common hydraulic structure; it consists of simple geometry, easier to be set in a model; it reproduces a challenging fully three-dimensional flow; and the results of physical model studies are available in literature.

OpenFOAM, a free and open source Computational Fluid Dynamics (CFD) software, was used in this research. This software has been widely used specially by academia, what may be explained by its no cost and its extended variety of tools and methods. Nevertheless, there are few studies applying this software to simulate open-channel flows and maybe nothing on confluences. Comparisons of velocity components were made from three turbulence models [the Re-Normalization Group (RNG) k-ε model, k-ω model, and a Large Eddy Simulation (LES) turbulence model]. The rigid lid approximation was adopted as the water-surface treatment method.

1.2 Goals

The study case that subsidize this research constitutes a very practical engineering work. It was not intended here to present new findings to the field of numerical modeling. Rather, in other to contribute to the scientific frontier, the scope is to evaluate the capabilities of a free and open CFD software also considering former model applications in the same theme.

1.2.1 General goal

The main goal of this research was to set up a three-dimensional numerical model and to evaluate its capability of reproducing the flow characteristics of a 90º open channel confluence, by comparing results obtained to published experimental data.

1.2.2 Specific goals

- To make a parametric study comparing the performance of different turbulence models – RNG k-Ɛ, k-ω and a LES; and
- To utilize OpenFOAM and evaluate its capabilities and user friendliness.

2 LITERATURE REVIEW

In the first subchapter here, it is intended to review some facts of the history of research on confluence and the development of its models. Later, two subchapters introduce the governing equations of fluid motion as well as important aspects of turbulent flows and turbulence models, what provide the mathematical basis for a comprehensive general-purpose CFD (Computational Fluid Dynamics) model. Lastly, a literature review is made about the application of CFD in industry and in confluences' studies.

2.1 Open-channel confluences

Confluences are present everywhere in natural landscapes or in urbanized areas. Both river junctions and prismatic open-channels, in canals in the country side or in urban water systems, present complex flow features governed by a large number of parameters. The systematic hydraulic treatment of a confluence cannot be made by applying simple theoretical equations as it is made in straight open-channels, since the effects of bottom slope and boundary roughness are of minor influence on the near flow field of a junction.

Weber *et al.* (2001) examined a 90° open-channel junction for channels of equal width in a physical model study that provided a high quality data set of 3D velocity, water-surface and turbulence measurements useful for understanding deeply the flow in a confluence and for validation of numerical models.

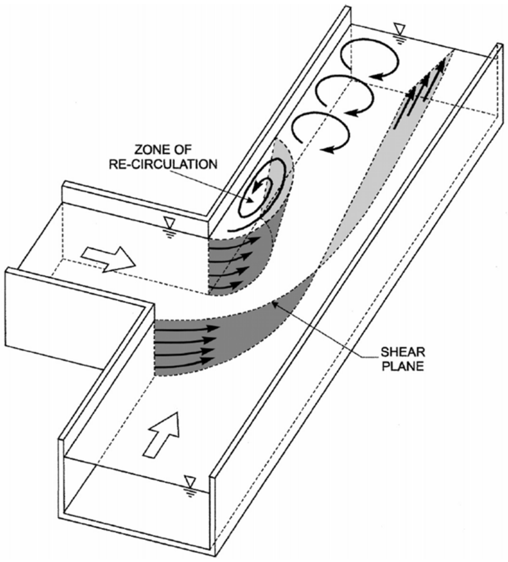

Figure 2.1: Schematic of flow structure in a subcritical confluence (Weber *et al.*, 2001)

The flow structure in the vicinity of the junction for a subcritical flow regime is shown schematically in Figure 2.1. The main characteristics of the flow patterns are: a separation zone with internal recirculation, high turbulence and lower water level just downstream the contribution of the branch; a resultant contracted section with higher velocities; a stagnation point nearby the upstream corner; a clockwise helicoidal along the downstream channel due to the reflectance of the side channel flow against the junction-opposite wall.

Much earlier, Taylor (1944) presented the first study on simple junction flow, with tests on 45° and 135° junctions of prismatic rectangular channels in subcritical conditions, and provided a momentum analysis that yields an equation for the depth ratio between the upstream branches and downstream channel.

Later, Webber & Greated (1966), by relating different flow variables, also provided predictive equations for the depth ratio in subcritical conditions (better accuracy than Taylor (1944)). In addition, they presented energy loss relationships and theoretical flow patterns by the method of conformal mapping.

Mamedov (1989) went further by making on-site investigations in a natural confluence on the Kura River (ancient Soviet Union, now Georgia) to study the characteristics and extent of channel deformation. The same author developed empirical methods of calculating the plan of the currents, stability of the channel, useful parameters of the contracted section (location, depth and average velocity) and the separation zone (length and width). In addition, laboratory experiments in a rectangular flume were conducted for a more detailed investigation of the problem of the effect of the angle of confluence and relationship of discharges in the confluence.

Gurram *et al.* (1997) also made laboratory experiments and provided expressions for the momentum correction coefficients, the lateral wall pressure force, and the ratio of the flow depths in the lateral and upstream branches of a subcritical confluence. In addition, a rational approach for the momentum contribution of the lateral branch was presented and applied for the prediction of the backwater effect across a simple junction.

Many one-dimensional numerical models of open-channel networks apply mass conservation and energy conservation principles at the junctions. Since energy losses and differences in velocity heads are difficult to evaluate, the interior boundary conditions may simply diminish to the equality of water-surface elevation and the continuity of discharge. HEC-RAS, maybe the most popular and free one-dimensional numerical model, also gives the option of applying the conservation of momentum, instead of energy conservation, but it still assumes equality of upstream depths. In order to fill this gap, Shabayek *et al.* (2002) developed a 1D model that does not assume equality of the upstream depths by applying mass and momentum conservation and considering an improved set of internal boundary conditions

These analytical and empirical models (Taylor, 1944; Webber & Greated, 1966; Gurram *et al.,* 1997; and Shabayek *et al.*, 2002) are useful to be applied in one-dimensional numerical models of open-channel networks, where the interest is in reproducing the free-surface profile in the channels with some approximation. However, no matter how advanced these 1D models are, when the interest is in understanding the flow behavior at the vicinity of the junction, it is clear that it becomes necessary to apply 2D or 3D numerical models.

2.2 Conservation laws of fluid motion

The equations presented in this subchapter are the classic governing equations of fluid motion analyzed three-dimensionally. This subchapter is based almost entirely on the content presented in chapter 2 of Versteeg & Malalasekera (2007). The main fluid properties are noted as $\mathbf{u}$, u, v, w, ρ, p, and τ, for the velocity vector, scalar velocities in the x-, y-, and z-direction, density, pressure, and viscous stresses, respectively. The governing equations of fluid flow represent mathematical statements of the conservation laws of physics:

- The mass of a fluid is conserved – what leads to the mass conservation equation
- The rate of change of momentum equals the sum of the forces on a fluid particle (Newton’s second law) – what leads to the momentum equation
- The rate of change of energy is equal to the sum of the rate of heat addition to and the rate of work done on a fluid particle (first law of thermodynamics) – what leads to the energy equation

According to Versteeg & Malalasekera (2007), liquids and gases flowing at low speeds behave as incompressible fluids. Without density variation there is no linkage between the energy equation and the mass conservation and momentum equations. The flow field can often be solved by considering mass conservation and momentum equations only. Since this is the case treated in this research, and the water temperature was held constant, the energy equation is not treated here.

2.2.1 Mass conservation in three dimensions

The first step in the derivation of the mass conservation equation is to write down a mass balance of the fluid element:

<u>Rate of increase of mass in fluid element = Net rate of flow of mass into fluid element</u>

The rate of increase of mass in the fluid element is:

$$\frac{\partial}{\partial t}(\rho\delta x\delta y\delta z)=\frac{\partial\rho}{\partial t}\delta x\delta y\delta z \qquad 2.1$$

The mass flow rate across a face of the element is given by the product of density, area and the velocity component normal to the face, as illustrated in Figure 2.2.

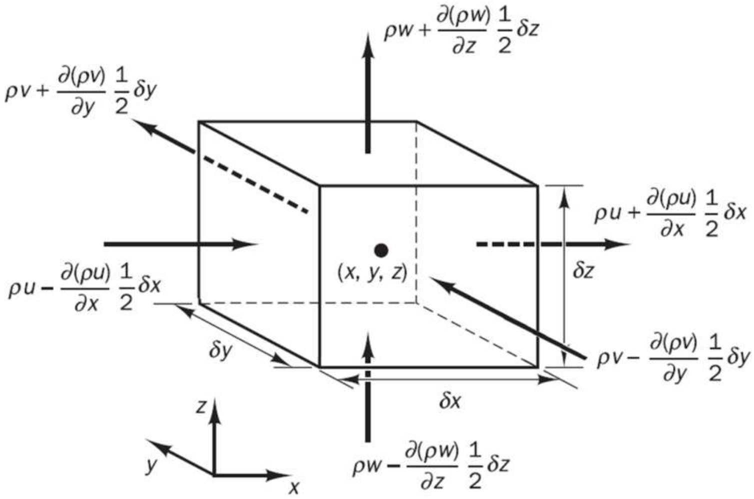

Figure 2.2: Mass flows in and out of fluid element (Versteeg & Malalasekera, 2007)

If all components are summed up, arranged and equated to equation 2.1, it is yielded the unsteady, three-dimensional mass conservation or continuity equation at a point in a compressible fluid:

$$\frac{\partial \rho}{\partial t}+\frac{\partial(\rho u)}{\partial x}+\frac{\partial(\rho v)}{\partial y}+\frac{\partial(\rho w)}{\partial z}=0 \qquad or \qquad \frac{\partial \rho}{\partial t}+div(\rho \boldsymbol{u})=0 \tag{2.2}$$

For an incompressible fluid, e.g. the water flow in a confluence as studied in this research, the density ρ is constant and equation 2.2 becomes:

$$\frac{\partial u}{\partial x}+\frac{\partial v}{\partial y}+\frac{\partial w}{\partial z}=0 \qquad or \qquad div\,\boldsymbol{u}=0 \tag{2.3}$$

2.2.2 Momentum equation in three dimensions

Newton's second law states that:

Rate of increase of momentum of fluid particle = Sum of forces on fluid particle

The rate of increase of x-momentum per unit volume of a fluid particle is:

$$\rho\left(\frac{\partial u}{\partial t}+u\frac{\partial u}{\partial x}+v\frac{\partial u}{\partial y}+w\frac{\partial u}{\partial z}\right)=\rho\,\frac{\partial u}{\partial t}+div(u\boldsymbol{u})=\rho\frac{Du}{Dt} \tag{2.4}$$

The rates of increase in the y- and z-direction can be found similarly. There are two types of forces on fluid particles: surface forces (pressure and viscous forces) and body forces (gravity, centrifugal, Coriolis and electromagnetic forces). It is common practice to highlight the contributions due to the surface forces as separate terms in the momentum equation and to include the effects of body forces as source terms. The state of stress of a fluid element is defined in terms of pressure and the nine viscous stresses components shown in Figure 2.3.

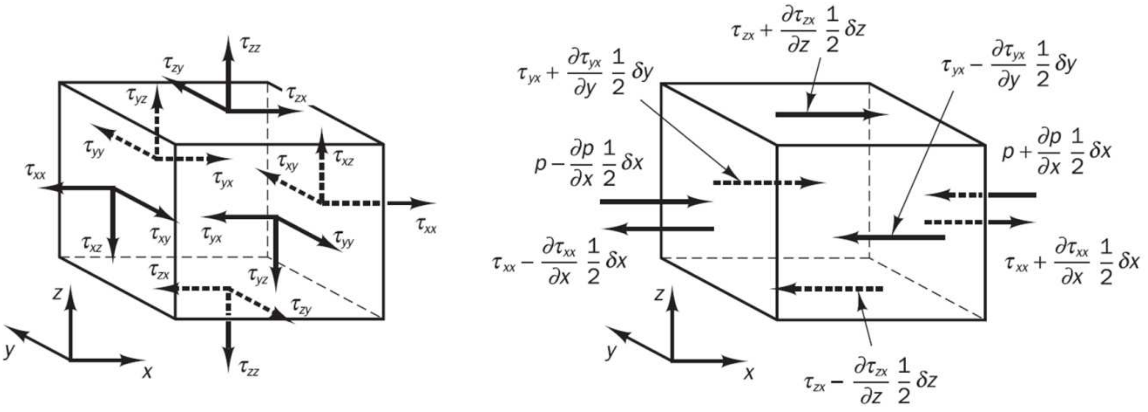

(a) (b)

Figure 2.3: Stress components on all faces of a fluid element, (a) in all directions, and (b) in the x-direction (Versteeg & Malalasekera, 2007)

The magnitude of a force resulting from a surface stress is the product of stress and area. The total force per unit volume on the fluid due to the surface stresses in the x-direction is:

$$\frac{\partial(-p+\tau_{xx})}{\partial x}+\frac{\partial\left(\tau_{yx}\right)}{\partial y}+\frac{\partial(\tau_{zx})}{\partial z} \qquad 2.5$$

Without considering the body forces, such as gravity and Coriolis forces, in further detail their overall effect can be included by defining a source S_{Mx} of x-momentum per unit volume per unit time.

So, the x-component of momentum equation is found by setting equation 2.4 equal to equation 2.5, plus S_{Mx}:

$$\rho\frac{Du}{Dt}=\frac{\partial(-p+\tau_{xx})}{\partial x}+\frac{\partial(\tau_{yx})}{\partial y}+\frac{\partial(\tau_{zx})}{\partial z}+S_{Mx} \qquad 2.6$$

In the same way, the y-component of the momentum equation is obtained:

$$\rho\frac{Dv}{Dt}=\frac{\partial(\tau_{xy})}{\partial x}+\frac{\partial(-p+\tau_{yy})}{\partial y}+\frac{\partial(\tau_{zy})}{\partial z}+S_{My} \qquad 2.7$$

and the z-component of the momentum equation is given by:

$$\rho\frac{Dw}{Dt}=\frac{\partial(\tau_{xz})}{\partial x}+\frac{\partial(\tau_{yz})}{\partial y}+\frac{\partial(-p+\tau_{zz})}{\partial z}+S_{Mz} \qquad 2.8$$

2.2.3 Navier-Stokes equations for a Newtonian fluid

The governing equations contain as further unknowns as the viscous stress components τ_{ij}. The most useful forms of the conservation equations for fluid flows are obtained by introducing a suitable model for the viscous stresses, τ_{ij}. All gases and many liquids are isotropic, so in these cases the viscous stresses can be expressed as functions of the local deformation rate or strain rate, which has nine components in three dimensions, comprised of three linear elongating deformation components:

$$s_{xx}=\frac{\partial u}{\partial x} \qquad s_{yy}=\frac{\partial v}{\partial y} \qquad s_{zz}=\frac{\partial w}{\partial z} \qquad 2.9$$

and six shearing linear deformation components, independent in isotropic fluids:

$$s_{xy} = s_{yx} = \frac{1}{2}\left(\frac{\partial u}{\partial y} + \frac{\partial v}{\partial x}\right) \qquad s_{xz} = s_{zx} = \frac{1}{2}\left(\frac{\partial u}{\partial z} + \frac{\partial w}{\partial x}\right) \qquad s_{zy} = s_{yz} = \frac{1}{2}\left(\frac{\partial w}{\partial y} + \frac{\partial v}{\partial z}\right)$$

2.10

The volumetric deformation is given by:

$$\frac{\partial u}{\partial x} + \frac{\partial v}{\partial y} + \frac{\partial u}{\partial z} = div\, \boldsymbol{u}$$

2.11

In a Newtonian fluid the viscous stresses are proportional to the rates of deformation. The three-dimensional form of Newton's law of viscosity for compressible flows involves two constants of proportionality: the first (dynamic) viscosity, μ, to relate to linear deformations, and the second viscosity, λ, to relate stresses to the volumetric deformation, usually approximated to $\lambda = -\frac{2}{3}\mu$ (Schlichting, 1979). The nine viscous stress components become:

$$\tau_{xx} = 2\mu\frac{\partial u}{\partial x} + \lambda\, div\, \boldsymbol{u} \qquad \tau_{yy} = 2\mu\frac{\partial v}{\partial y} + \lambda\, div\, \boldsymbol{u} \qquad \tau_{zz} = 2\mu\frac{\partial w}{\partial z} + \lambda\, div\, \boldsymbol{u}$$

$$\tau_{xy} = \tau_{yx} = \mu\left(\frac{\partial u}{\partial y} + \frac{\partial v}{\partial x}\right) \qquad \tau_{xz} = \tau_{zx} = \mu\left(\frac{\partial u}{\partial z} + \frac{\partial w}{\partial x}\right) \qquad \tau_{yz} = \tau_{zy} = \mu\left(\frac{\partial v}{\partial z} + \frac{\partial w}{\partial y}\right)$$

2.12

Substituting equations 2.12 into equations 2.6 - 2.8 yields the Navier-Stokes equations (for compressible fluids with variable viscosity):

$$\rho\frac{Du}{Dt} = -\frac{\partial p}{\partial x} + \frac{\partial}{\partial x}\left[2\mu\frac{\partial u}{\partial x} + \lambda\, div\, \boldsymbol{u}\right] + \frac{\partial}{\partial y}\left[\mu\left(\frac{\partial u}{\partial y} + \frac{\partial v}{\partial x}\right)\right] + \frac{\partial}{\partial z}\left[\mu\left(\frac{\partial u}{\partial z} + \frac{\partial w}{\partial x}\right)\right] + S_{Mx}$$

$$\rho\frac{Dv}{Dt} = -\frac{\partial p}{\partial y} + \frac{\partial}{\partial x}\left[\mu\left(\frac{\partial u}{\partial y} + \frac{\partial v}{\partial x}\right)\right] + \frac{\partial}{\partial y}\left[2\mu\,\frac{\partial v}{\partial y} + \lambda\, div\, \boldsymbol{u}\right] + \frac{\partial}{\partial z}\left[\mu\left(\frac{\partial v}{\partial z} + \frac{\partial w}{\partial y}\right)\right] + S_{My}$$

$$\rho\frac{Dw}{Dt} = -\frac{\partial p}{\partial z} + \frac{\partial}{\partial x}\left[\mu\left(\frac{\partial u}{\partial z} + \frac{\partial w}{\partial x}\right)\right] + \frac{\partial}{\partial y}\left[\mu\left(\frac{\partial v}{\partial z} + \frac{\partial w}{\partial y}\right)\right] + \frac{\partial}{\partial z}\left[2\mu\frac{\partial w}{\partial z} + \lambda.div\, \boldsymbol{u}\right] + S_{Mz}$$

2.13

In the case studied in this research, the flow is considered incompressible, so the mass conservation equation is div $\mathbf{u} = 0$. Additionally, the viscosity is adopted as constant. Hence, the Navier-Stokes equations can be simplified to:

$$\rho\frac{Du}{Dt} = -\frac{\partial p}{\partial x} + \mu\left(\frac{\partial^2 u}{\partial x^2} + \frac{\partial^2 u}{\partial y^2} + \frac{\partial^2 u}{\partial z^2}\right) + S_{Mx} = -\frac{\partial p}{\partial x} + \mu\, div(grad\ (u)) + S_{Mx}$$

$$\rho \frac{Dv}{Dt} = -\frac{\partial p}{\partial y} + \mu \left(\frac{\partial^2 v}{\partial x^2} + \frac{\partial^2 v}{\partial y^2} + \frac{\partial^2 v}{\partial z^2} \right) + S_{My} = -\frac{\partial p}{\partial y} + \mu \, div(grad\ (v)) + S_{My}$$

$$\rho \frac{Dw}{Dt} = -\frac{\partial p}{\partial z} + \mu \left(\frac{\partial^2 w}{\partial x^2} + \frac{\partial^2 w}{\partial y^2} + \frac{\partial^2 w}{\partial z^2} \right) + S_{Mz} = -\frac{\partial p}{\partial z} + \mu \, div(grad\ (w)) + S_{Mz}$$

2.14

It is clear from the equations 2.2 and 2.14 that there are significant commonalities among the various equations. Accordingly, a general transport equation for incompressible fluids can be written in the form:

$$\frac{\partial \phi}{\partial t} + div(\phi \boldsymbol{u}) = \frac{1}{\rho} \, div\big(\Gamma_\phi \, grad\ (\phi)\big) + S_\phi$$

2.15

Versteeg & Malalasekera (2007) described this equation in words as:

Rate of increase of ϕ of fluid element (rate of change term)	+	*Net rate of flow of ϕ out of fluid element (convective term)*	=	*Rate of increase of ϕ due to diffusion (diffusion term)*	+	*Rate of increase of ϕ due to sources (source term)*

2.3 Turbulence

A flow is laminar when it is smooth and adjacent layers of fluid slide past each other in an orderly fashion, what can be expressed by values below the so-called critical Reynolds number Re_{crit}. At values of the Reynolds number above Re_{crit}, the flow behavior becomes chaotic and random, what is defined as turbulent flow.

Velocity gradients, i.e. velocity differences between adjacent layers, are one of originators of turbulence. Figure 2.4 illustrates a flow transitioning from an incoming laminar flow to a fully developed turbulent one. Due to friction, velocities closer to the plate decrease and viscous stresses appear generating turbulent kinetic energy.

Turbulent fluctuations always have three-dimensional spatial character (Versteeg & Malalasekera, 2007). Visualizations of turbulent flows reveal rotational flow structures, so-called turbulent eddies. These vortices have the capability of transporting and exchanging heat, mass and momentum by diffusion. They range from very large eddies, i.e. at the size of the shear flow which creates the primary vortex structures, until very small ones.

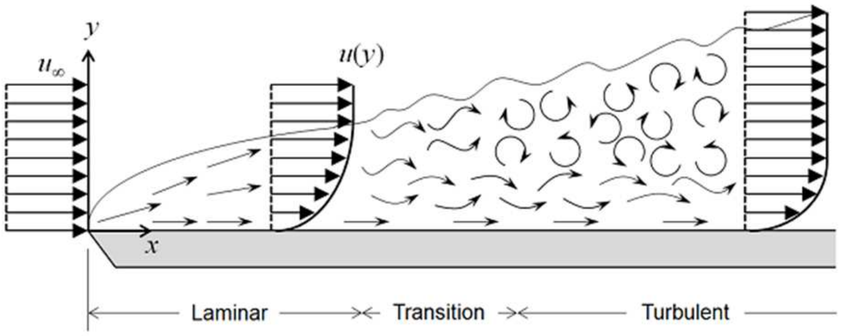

Figure 2.4: Longitudinal view sketch of transition processes in boundary layer flow over a flat plate (adapted from Frei, 2013)

By the break-up process, kinetic energy is transferred from larger structures to smaller and smaller ones, in a process called energy cascade. The larger eddies are the most energetic, for they acquire their energy through strong interactions with the mean flow. The smallest eddies present a local Reynolds number equal to 1, i.e. the inertia and viscous effects are of equal strength. At these smaller scales, work is performed against the action of viscous stresses, so that the energy associated with small-scale eddy motions is dissipated and converted into thermal internal energy. Therefore, the more turbulent the flow is, the more energy dissipation occurs.

According to Schlichting (1979), flows in the laminar regime, with low Reynolds number, are completely described by the continuity and the Navier-Stokes equations. Simple laminar flows can be analytically solved, while more complex laminar flows should be solved numerically with CFD techniques without additional approximations. In most practical engineering applications, however, the flow presents higher Reynolds numbers where turbulence is observed. In these cases, fluid engineers need access to viable tools capable of representing the effects of turbulence. Turbulence models can be grouped into the following three categories:

- Turbulence models for Reynolds-Averaged Navier-Stokes (RANS) equations: Navier-Stokes equations are time averaged, and its resulting extra terms, related to turbulent fluctuations, are solved by classical models as the k-ε model and the Reynolds Stress Model (RSM).
- Large Eddy Simulation (LES): It tracks the behavior of larger eddies through space filtering of the Navier-Stokes equations prior to computations. Unsteady flow

equations have to be solved, increasing the computational costs, but it has already been used to address CFD problems with complex geometries.

- Direct Numerical Simulation (DNS): It computes the mean flow and all turbulent velocity fluctuations. It is highly costly in terms of computing resources, unfeasible for industrial flow computations.

The first two groups will be treated here, since they are directly related to the object of this research.

2.3.1 Turbulence models for Reynolds-Averaged Navier-Stokes equations

In turbulent flow regime, the motion is intrinsically unsteady even with imposed boundary conditions and the velocity and all other flow properties vary in a random and chaotic way. If the velocity is measured at a point in such a flow, a typical time-series graph is obtained as represented in Figure 2.5.

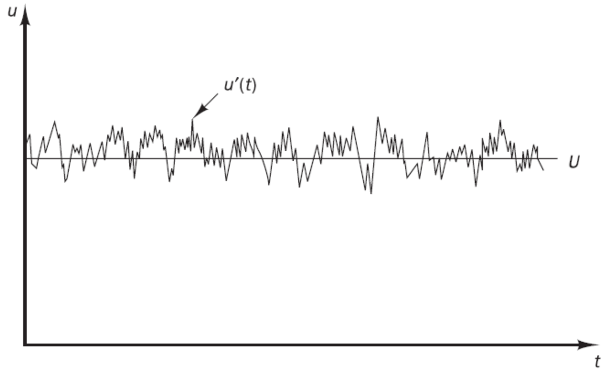

Figure 2.5: Typical point velocity measurement in turbulent flow (Versteeg & Malalasekera, 2007)

For most engineering purposes the details of the turbulent fluctuations of the flow is not necessary to be known, as only the mean properties matter. Through the so called Reynolds Decomposition, a turbulent flow can be characterized in terms of the mean values of flow properties (denoted in upper case symbols: U, V, W, P, Φ etc.) and their deviation (or fluctuation) from the mean (denoted as: u’, v’, w’, p’, ϕ’ etc.). Note that the fluctuating part has a mean value equal to 0. In a general form:

$$\phi(t) = \Phi + \phi'(t) \tag{2.16}$$

Considering the continuity equation 2.3, it can be noted that div **u** = div **U**, what yields the continuity equation for the mean flow:

$$div\ U = 0$$

2.17

Time-averaging the Navier-Stokes equations 2.14 and rearranging the extra terms of fluctuating velocities, it is obtained the Reynolds-Averaged Navier-Stokes (RANS) equations for incompressible flow:

$$\frac{\partial U}{\partial t} + div(U\boldsymbol{U}) = -\frac{1}{\rho}\frac{\partial P}{\partial x} + \nu\ div(grad(U)) + \frac{1}{\rho}\left[\frac{\partial\left(-\rho\overline{u'^2}\right)}{\partial x} + \frac{\partial(-\rho\overline{u'v'})}{\partial y} + \frac{\partial(-\rho\overline{u'w'})}{\partial z}\right]$$

$$\frac{\partial V}{\partial t} + div(V\boldsymbol{V}) = -\frac{1}{\rho}\frac{\partial P}{\partial y} + \nu\ div(grad(V)) + \frac{1}{\rho}\left[\frac{\partial(-\rho\,\overline{u'v'})}{\partial x} + \frac{\partial\left(-\rho\overline{v'^2}\right)}{\partial y} + \frac{\partial(-\rho\overline{v'w'})}{\partial z}\right]$$

$$\frac{\partial W}{\partial t} + div(W\boldsymbol{W}) = -\frac{1}{\rho}\ \frac{\partial P}{\partial z} + \nu\ div(grad(W)) + \frac{1}{\rho}\left[\frac{\partial(-\rho\overline{u'w'})}{\partial x} + \frac{\partial(-\rho\overline{v'w'})}{\partial y} + \frac{\partial\left(-\rho\overline{w'^2}\right)}{\partial z}\right]$$

2.18

The fluctuating velocity terms are associated to the so-called Reynolds stress, comprised of: a) three normal stresses

$$\tau_{xx} = -\rho\overline{u'^2} \qquad \tau_{yy} = -\rho\overline{v'^2} \qquad \tau_{zz} = -\rho\overline{w'^2}$$

2.19

and b) three shear stresses

$$\tau_{xy} = \tau_{yx} = -\rho\overline{u'v'} \qquad \tau_{xz} = \tau_{zx} = -\rho\overline{u'w'} \qquad \tau_{yz} = \tau_{zy} = -\rho\overline{v'w'}$$

2.20

By the Boussinesq assumption, the Reynolds stresses are proportional to the rates of deformation. Using a suffix notation, it can be expressed as:

$$\tau_{ij} = -\rho\overline{u_i'u_j'} = \mu_t\left(\frac{\partial U_i}{\partial x_j} + \frac{\partial U_j}{\partial x_i}\right) - \frac{2}{3}\rho k\delta_{ij} = \mu_t S_{ij} - \frac{2}{3}\rho k\delta_{ij}$$

2.21

With: $\delta_{ij} = 1$ if i = j, and $\delta_{ij} = 0$ if i ≠ j.

Similar extra turbulent transport terms arise when equation 2.15 is derived, considering an arbitrary scalar quantity, $\phi(t) = \Phi + \phi'(t)$:

$$\frac{\partial \Phi}{\partial t} + div(\Phi \boldsymbol{U}) = \frac{1}{\rho} div(\Gamma_{\Phi} grad(\Phi)) + \frac{1}{\rho}\left[\frac{\partial\left(-\rho\overline{u'\phi'}\right)}{\partial x} + \frac{\partial(-\rho\overline{v'\phi'})}{\partial y} + \frac{\partial(-\rho\overline{u'\phi'})}{\partial z}\right] + S_{\Phi} \tag{2.22}$$

Now it is necessary to apply turbulence models to predict Reynolds stresses and the scalar transport terms and close the system formed by mean flow equations 2.17, 2.18 and 2.22. The most common RANS turbulence models are shown in Table 2-1, classified based on the number of additional transport equations needed to be solved along with the RANS flow equations.

Table 2-1: Most common turbulence models classified by extra transport equations

No. of extra transport equations	Name
Zero	Mixing length model
One	Spalart-Allmaras model
Two	k-ε model
	k-ω model
	Algebraic stress model
Seven	Reynolds Stress Model

On this research a variation of the k-ε and the k-ω models were applied (as well as a LES model) to calculate the flow in a confluence. Therefore, they are described briefly as it follows.

2.3.1.1 The k-ε model

The instantaneous kinetic energy, k(t), of a turbulent flow can be also decomposed as: $\mathrm{k(t)} = \mathrm{K} + \mathrm{k}$, for the mean kinetic energy, $\mathrm{K} = \frac{1}{2}(\mathrm{U}^2 + \mathrm{V}^2 + \mathrm{W}^2)$, and the turbulent kinetic energy, $\mathrm{k} = \frac{1}{2}\left(\overline{\mathrm{u}'^2} + \overline{\mathrm{v}'^2} + \overline{\mathrm{w}'^2}\right)$.

The mean kinetic energy equation is obtained by multiplying the mean velocity component U, V or W by the x-, y- or z-component of RANS equation (2.18), respectively. After adding the results and a good effort on rearranging the terms, it can be obtained the time-averaged equation governing the mean kinetic energy of the flow:

$$\frac{\partial(\rho K)}{\partial t} + div(\rho K \boldsymbol{U}) = div\left(-PU + 2\mu \boldsymbol{U} S_{ij} - \rho \boldsymbol{U}\overline{u_i' u_j'}\right) - 2\mu S_{ij}.S_{ij} + \rho\overline{u_i' u_j'}.S_{ij} \tag{2.23}$$

The turbulent kinetic energy equation can be yielded, not simply, by the multiplication of each of the instantaneous Navier-Stokes equations (2.14) by the appropriate fluctuating velocity components and addition of all the results, followed by a repeat of this process on the RANS equations (2.18), subtraction of the two resulting equations and very substantial rearrangement (Versteeg & Malalasekera, 2007):

$$\frac{\partial(\rho k)}{\partial t} + div(\rho k\boldsymbol{U}) = div\left(-\overline{p'u'} + 2\mu\overline{\boldsymbol{u}'s'_{ij}} - \rho\frac{\mathbf{1}}{\mathbf{2}}\overline{u'_{ij}.u'_{ij}u'_{ij}}\right) - 2\mu\overline{s'_{ij}.s'_{ij}} - \rho\overline{u'_{ij}u'_{ij}}.S_{ij} \tag{2.24}$$

Versteeg & Malalasekera (2007) described this equation in words as:

Rate of change of turbulent kinetic energy k	+	*Transport of k by convection*	=	*Transport of k by pressure*	+	*Transport of k by viscous stress*	+	*Transport of k by Reynolds stress*	-	*Rate of dissipation of k*	+	*Rate of production of k*

The rate of dissipation per unit volume is normally written as the product of the density, ρ, and the rate of dissipation of turbulent kinetic energy per mass, ε, so:

$$\varepsilon = 2\nu\overline{s'_{ij}.s'_{ij}} \tag{2.25}$$

This property is the destruction term in the turbulent kinetic energy equation, of the same order of magnitude as the production term. When the Reynolds number is high, the viscous transport term is always very small compared with the turbulence transport term and the dissipation (Versteeg & Malalasekera, 2007).

The standard k-ε model (Launder & Spalding, 1974) was developed from the simplistic concept that k and ε are related to a velocity scale, ϑ, and a length scale, ℓ, according to:

$$\vartheta = k^{1/2} \tag{2.26}$$

$$\ell = \frac{k^{3/2}}{\varepsilon} \tag{2.27}$$

Using these equations, by dimensional analysis, the eddy viscosity can be described as:

$$\mu_t = C\rho\vartheta\ell \tag{2.28}$$

Finally, the standard k-ε model transport equations are developed to:

$$\frac{\partial(\rho k)}{\partial t}+div(\rho k\boldsymbol{U})=div\left(\frac{\mu_t}{\sigma_k}grad(k)\right)+2\mu_t S_{ij}.S_{ij}-\rho\varepsilon$$

2.29

$$\frac{\partial(\rho\varepsilon)}{\partial t}+div(\rho\varepsilon\boldsymbol{U})=div\left(\frac{\mu_t}{\sigma_\varepsilon}grad(\varepsilon)\right)+C_{1\varepsilon}\frac{\varepsilon}{k}2\mu_t S_{ij}.S_{ij}-C_{2\varepsilon}\rho\frac{\varepsilon^2}{k}$$

2.30

In words,

$$\begin{matrix}\textit{Rate of change} \\ \textit{of } k \textit{ or } \varepsilon\end{matrix} + \begin{matrix}\textit{Transport of } k \textit{ or} \\ \varepsilon \textit{ by convection}\end{matrix} = \begin{matrix}\textit{Transport of } k \\ \textit{or } \varepsilon \textit{ by diffusion}\end{matrix} + \begin{matrix}\textit{Rate of production} \\ \textit{of } k \textit{ or } \varepsilon\end{matrix} - \begin{matrix}\textit{Rate of destruction} \\ \textit{of } k \textit{ or } \varepsilon\end{matrix}$$

Some adjustable empirical constants were used in these equations:

$$C_\mu=0{,}09 \qquad \sigma_k=1{,}00 \qquad \sigma_\varepsilon=1{,}30 \qquad C_{1\varepsilon}=1{,}44 \qquad C_{2\varepsilon}=1{,}92$$

2.31

The k-ε model is the most widely used and validated turbulence model, used with reasonable accuracy in a general-purpose way. Nevertheless, some critics were raised to the standard k-ε model especially about the strong linkage between production and destruction of turbulent kinetic energy, what says that the dissipation rate ε is large where production of k is large. This behavior happens in confined flows, but it does not happen in some unconfined flows, or flows with large extra strains, or rotating flows.

In response to that, some advanced two-equation turbulence models were developed. Yakhot *et al.* (1992) devised the renormalization group (RNG) k-ε model equations for high Reynolds number flows:

$$\frac{\partial(\rho k)}{\partial t}+div(\rho k\boldsymbol{U})=div\big(\alpha_k\mu_{eff}grad(k)\big)+\tau_{ij}.S_{ij}-\rho\varepsilon$$

2.32

$$\frac{\partial(\rho\varepsilon)}{\partial t}+div(\rho\varepsilon\boldsymbol{U})=div\big(\alpha_\varepsilon\mu_{eff}grad(\varepsilon)\big)+C_{1\varepsilon}^{*}\frac{\varepsilon}{k}\tau_{ij}.S_{ij}-C_{2\varepsilon}\rho\frac{\varepsilon^2}{k}$$

2.33

With:

$$\mu_{eff}=\mu+\mu_t \qquad \mu_t=\rho C_\mu\frac{k^2}{\varepsilon}$$

2.34

$$C_\mu=0{,}0845 \qquad \alpha_k=\alpha_\varepsilon=1{,}39 \qquad C_{1\varepsilon}=1{,}42 \qquad C_{2\varepsilon}=1{,}68$$

$$C_{1\varepsilon}^{*}=C_{1\varepsilon}-\frac{\eta(1-\eta/\eta_0)}{1+\beta\eta^3} \qquad \eta=\frac{k}{\varepsilon}\sqrt{2S_{ij}.S_{ij}} \qquad \eta_0=4{,}377 \qquad \beta=0{,}012$$

2.35

They consist of a variation of the standard k-ε model equations that systematically removes the small scales of motion from the governing equations by expressing their effects in terms of larger scale motions and a modified viscosity (Versteeg & Malalasekera, 2007). It is interesting to note that the model changes the ε equations also by containing a strain-dependent correction term in the constant $C_{1\varepsilon}$ of the production term.

2.3.1.2 The k-ω model

The most prominent alternative to trying to overcome some limitations of the k-ε model (and variants) is the k-ω model, which is also a two-equation turbulence model, developed by Wilcox (1988). As the name says, besides the variable k, it uses the turbulence frequency ω = ε / k as the second variable. Then the eddy viscosity becomes:

$$\mu_t = \rho k/\omega \tag{2.36}$$

And the transport equations for k and ω for high Reynolds turbulent flows are developed as:

$$\frac{\partial(\rho k)}{\partial t} + div(\rho k\boldsymbol{U}) = div\left[\left(\mu + \frac{\mu_t}{\sigma_k}\right) grad(k)\right] + P_k - \beta^* \rho k\omega \tag{2.37}$$

With: $$P_k = \left(2\mu_t S_{ij}.S_{ij} - \frac{2}{3}\rho k \frac{\partial U_i}{\partial x_j}\delta_{ij}\right) \tag{2.38}$$

And: $$\frac{\partial(\rho\omega)}{\partial t} + div(\rho\omega\boldsymbol{U}) = div\left[\left(\mu + \frac{\mu_t}{\sigma_\omega}\right) grad\ (\omega)\right] + \gamma_1\left(2\rho S_{ij}.S_{ij} - \frac{2}{3}\rho\omega\frac{\partial U_i}{\partial x_j}\delta_{ij}\right) - \beta_1 \rho\omega^2 \tag{2.39}$$

In words,

Rate of change of k or ω + *Transport of k or ω by convection* = *Transport of k or ω by diffusion* + *Rate of production of k or ω* - *Rate of destruction of k or ω*

The adjustable empirical constants are:

$\sigma_k = 2{,}0$ $\sigma_\omega = 2{,}0$ $\gamma_1 = 0{,}553$ $\beta_1 = 0{,}075$ $\beta^* = 0{,}09$

It is not really clear in literature whether the k-ω model is more suitable for general purposes than the k-ε model. Versteeg & Malalasekera (2007) says that the k-ω has a similar range of strengths and weaknesses as the k-ε model and fails to include accounts of more subtle interactions between turbulent stresses and mean flow when compared with the RSM.

Nevertheless the computational costs of the RSM are significantly higher, since it is necessary to solve 7 extra turbulence equations.

2.3.2 Large-Eddy Simulation

A different approach to the simulation of turbulent flows is the Large Eddy Simulation (LES). Its idea is that the larger eddies need to be computed for each problem with time-dependent simulation.

Through a decomposition, a flow variable can be characterized as the sum of (i) the filtered function ($\bar{u}$, $\bar{v}$, $\bar{w}$, $\bar{p}$ etc.) with spatial variations that are larger than the cutoff width and are resolved by the LES computation, and (ii) the unresolved spatial variations (u', v', w', p' etc.) at a length scale smaller than the filter cutoff width. In a general form:

$$\phi(x,t) = \bar{\phi}(x,t) + \phi'(x,t) \tag{2.40}$$

Instead of time-averaging (as in the RANS turbulence models) LES uses a spatial filtering operation (indicated by the overbar) to separate the larger and smaller eddies.

The initial procedures consist in selecting the filtering function and a certain cutoff width that separates the information related to the larger eddies (to be resolved) from the smaller turbulent eddies (to be rejected and destroyed). The filter function is defined as G(**x**, **x**', Δ) applied in the following equation:

$$\bar{\phi}(\boldsymbol{x},t) = \int_{-\infty}^{\infty}\int_{-\infty}^{\infty}\int_{-\infty}^{\infty} G(\boldsymbol{x},\boldsymbol{x}',\Delta)\phi(\boldsymbol{x}',t)dx_1'dx_2'dx_3' \tag{2.41}$$

Where:

$\bar{\phi}(\mathbf{x},t) =$ filtered function

$\phi(\mathbf{x},t) =$ original (unfiltered) function

$\Delta =$ filter cutoff width

The cutoff width is intended as an indicative measure of the size of eddies that are retained in the computations and the eddies that are rejected. The most common selection is to take the cutoff width to be of the same order as grid size, or $\Delta = \sqrt[3]{\Delta x. \Delta y. \Delta z}$.

Filtering of equation 2.3 easily yields the LES continuity equation for incompressible flows:

$$div(\overline{\boldsymbol{u}}) = 0 \tag{2.42}$$

While filtering of equations 2.14 yields the LES Navier-Stokes equations for an incompressible flow:

$$\frac{\partial \bar{u}}{\partial t} + div(\bar{u}\overline{\boldsymbol{u}}) = -\frac{1}{\rho}\frac{\partial \bar{p}}{\partial x} + \nu\ div(grad(\bar{u})) - (div(\overline{u\boldsymbol{u}}) - div(\bar{u}\overline{\boldsymbol{u}}))$$

$$\frac{\partial \bar{v}}{\partial t} + div(\bar{v}\overline{\boldsymbol{u}}) = -\frac{1}{\rho}\frac{\partial \bar{p}}{\partial y} + \nu\ div(grad(\bar{v})) - (div(\overline{v\boldsymbol{u}}) - div(\bar{v}\overline{\boldsymbol{u}}))$$

$$\frac{\partial \bar{v}}{\partial t} + div(\bar{w}\overline{\boldsymbol{u}}) = -\frac{1}{\rho}\frac{\partial \bar{p}}{\partial z} + \nu\ div(grad(\bar{w})) - (div(\overline{w\boldsymbol{u}}) - div(\bar{w}\overline{\boldsymbol{u}}))$$

(I) (II) (III) (IV) (V)

2.43

Versteeg & Malalasekera (2007) name the terms of these equations as: (I) the rate of change of filtered x-, y- and z-momentum; (II) and (IV) the convective and diffusive fluxes of filtered x-, y- and z-momentum; (III) the gradients in the x-, y- and z-directions of the filtered pressure field; and (V) the extra terms caused by the filtering operation (just like the Reynolds stresses in the RANS equations that arouse as a consequence of time-averaging). The last terms (V) can be considered as a divergence of a set of stresses τ_{ij}, written as:

$$(div(\rho\overline{u_i\boldsymbol{u}} - \rho\bar{u}_i\overline{\boldsymbol{u}}) = \frac{\partial(\rho\overline{u_i u} - \rho\bar{u}_i\bar{u})}{\partial x} + \frac{\partial(\rho\overline{u_i v} - \rho\bar{u}_i\bar{v})}{\partial y} + \frac{\partial(\rho\overline{u_i w} - \rho\bar{u}_i\bar{w})}{\partial z} = \frac{\partial \tau_{ij}}{\partial x_j} \tag{2.44}$$

Where:

$$\tau_{ij} = \rho\overline{u_i\boldsymbol{u}} - \rho\bar{u}_i\overline{\boldsymbol{u}} = \rho\overline{u_i u_j} - \rho\bar{u}_i\bar{u}_j \tag{2.45}$$

These stresses are normally called the LES Sub-Grid-Scale (SGS) stresses. Using the decomposition equation 2.40 into equation 2.45, the SGS stresses are obtained:

$$\tau_{ij} = \left(\rho\overline{\bar{u}_i\bar{u}_j} - \rho\bar{u}_i\bar{u}_j\right) + (\rho\overline{\bar{u}_i u'_j} + \rho\overline{u'_i\bar{u}_j}) + \rho\overline{u'_i u'_j}$$

(I) (II) (III)

2.46

The SGS stresses contain three groups of contributions: the Leonard stresses (I), due to the effects at resolved scale; the cross-stresses (II), due to interactions between the SGS eddies and the resolved flow; and the LES Reynolds stresses (III), caused by convective momentum transfer due to interactions of SGS eddies.

Just like the Reynolds stresses in the RANS equations, the SGS stresses (equation 2.46) must be modeled. Detailed information about these models is present by Chai & Mahesh (2010) or by Versteeg & Malalasekera (2007).

The necessity to resolve unsteady equations makes LES much more costly computationally than the two-equation turbulence models. When compared with the RSM, however, this difference is very modest. For some cases where persistent large-scale vortices have a substantial influence on flow development, as in confluences, the accuracy of an LES model and its capability of reproducing some time-dependent features might be worth the price.

2.3.3 Law of the wall

Near solid walls, the flow behavior and turbulence structure are considerably different from free turbulent flows. The turbulent flow near solid boundaries is composed of four specific regions, as illustrated in Figure 2.6:

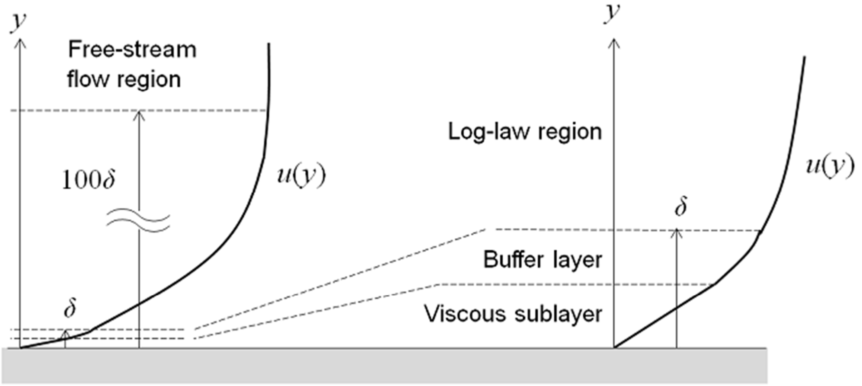

Figure 2.6: Typical mean velocity profile close to a solid boundary (Frei, 2013)

- Linear, laminar or viscous sub-layer: a very thin layer closer to the wall where the viscous forces dominate and the velocity varies linearly with distance from the wall, starting from 0 at the wall.
- Buffer layer: a thin region where the flow begins to transition to turbulent.

- Log-law layer: a fully turbulent region where the average velocity is related to the log of the distance to the wall.
- Free-stream region, or outer layer, or law-of-the-wake layer: a turbulent region where the gradient of the average velocity is zero.

Before representing the flow behavior in these layers, it is necessary to define the dimensionless velocity, u^+, and the dimensionless distance to the wall, y^+, as:

$$u^+ = \frac{U}{u_\tau} = f(y^+) \qquad y^+ = \frac{\rho u_\tau y}{\mu} \tag{2.47}$$

Where:
U = mean velocity
u_τ = shear velocity $= \sqrt{\tau_w/\rho}$
τ_w = shear stress at the wall $= \mu \frac{\partial U}{\partial y}$

According to Versteeg & Malalasekera (2007), the viscous sub-layer is in practice extremely thin, located at about $y^+ < 5$. By integrating the shear stress τ_w with respect to y and application of boundary condition U = 0 if y = 0, it is obtained a linear relationship between the mean velocity and the distance to the wall:

$$U = \frac{\tau_w y}{\mu} \tag{2.48}$$

Or, after some algebra, $u^+ = y^+$.

$$\tag{2.49}$$

In the log-law layer, $30 < y^+ < 500$ (Versteeg & Malalasekera, 2007), another relationship between u^+ and y^+ is derived:

$$u^+ = \frac{1}{\kappa} ln(Ey^+) \tag{2.50}$$

Where:
κ = von Karman’s constant ≈ 0,4
E = additive constant ≈ 9,8 (for smooth walls)

It is possible to compute the flow field in all four of these regimes. However, in order to avoid having to use a very refined mesh closer to the wall, the RANS as well as the LES turbulence models make use of wall functions, which relate the local wall shear stress to the mean velocity, turbulent kinetic energy and rate of dissipation.

More details on the phenomenon of turbulence are present in the works of Schlichting (1979), White (1991) and Versteeg & Malalasekera (2007).

2.4 CFD modeling

2.4.1 CFD in industry

Computational Fluid Dynamics, or CFD, is a branch of fluid mechanics that uses numerical methods and algorithms to solve mathematical models that describe any kind of fluid flow. In the words of Versteeg & Malalasekera (2007), CFD is the analysis of systems involving fluid flow, heat transfer and associated phenomena by means of computer-based simulation. The technique is very powerful and spans a wide range of industrial and non-industrial application areas. Some examples are:

- aerodynamics of aircraft and vehicles: lift and drag
- hydrodynamics of ships
- power plant: combustion in internal combustion engines and gas turbines
- turbo-machinery: flows inside rotating passages, diffusers etc.
- electrical and electronic engineering: cooling of equipment including microcircuits
- chemical process engineering: mixing and separation, polymer moulding
- external and internal environment of buildings: wind loading and heating/ventilation
- marine engineering: loads on off-shore structures
- environmental engineering: distribution of pollutants and effluents
- hydrology and oceanography: flows in rivers, estuaries, oceans
- hydraulics: flow in channels, weirs, locks and other hydraulic structures
- meteorology: weather prediction
- biomedical engineering: blood flows through arteries and veins

The availability of affordable high-performance computing hardware and the introduction of user-friendly interfaces have led to a recent upsurge of interest, and CFD has entered into the wider industrial community since the 1990s (Versteeg & Malalasekera, 2007).

CFD codes are structured around the numerical algorithms that can tackle fluid flow problems. In order to provide easy access to their solving power all commercial CFD packages include sophisticated user interfaces to input problem parameters and to examine the results. Hence all codes contain three main elements: (i) a pre-processor, (ii) a solver and (iii) a post-processor.

In solving fluid flow problems it is necessary to be aware that the underlying physics is complex and the results generated by a CFD code are at best as good as the physics (and chemistry) embedded in it and at worst as good as its operator.

It is impossible to assess the validity of the models of physics and chemistry embedded in a program as complex as a CFD code or the accuracy of its final results by any means other than comparison with experimental test work. Anyone wishing to use CFD in a serious way must realize that it is no substitute for experimentation, but a very powerful additional problem solving tool and crucial to reduce design costs.

2.4.2 CFD in confluences

Though the performance of a CFD model of a confluence is potentially great, its application to practical large-scale problems or open-channel networks is costly and in some cases unfeasible. With that in mind, one may choose to perform 2D models instead, which apply the governing equations of fluid motion in two dimensions averaging the parameters in the depth axis, becoming the formally known depth-averaged 2D shallow water flow equations.

Thanh *et al*. (2010) performed four different types of depth-averaged 2D models without and with effects of secondary current in a sharp-edge open-channel junction using the experimental data of Weber *et al.* (2001) for validation. The most distinctive features are captured by the models with effect of secondary current, indicating high applicability to an open-channel confluence flow in practice. Since, by definition, it does not reproduce 3D currents and vertical mixtures, further application for other problems such as sediment transport (not analyzed by them) might be a mere rough approximation.

A few three-dimensional numerical model studies of junctions have been performed and reported, each one testing different modeling tools and adding some interesting findings. Two researches performed numerical models in a prismatic rectangular open-channel confluence also using the physical model results of Weber *et al.* (2001) to validate them: Huang *et al.* (2002) and Dordevic (2012).

In literature there is perhaps no research that provides results of physical model studies of confluences as complete as that available from Weber *et al.* (2001). According to these authors, the collected data in previous studies are limited to 1D or 2D velocities and are often dependent on dye trace visualization for flow description. The data set presented comprised a fine grid of 3D velocity and turbulence measurements for six flow conditions along with water-surface mappings for four of these six conditions, constituting a benchmark very useful for the validation of 3D CFD models.

The following graphs show the different types of experimental data provided: longitudinal velocity distributions (u*, nondimensionalized by the outlet average velocity, U_t = 0,628 m/s, as in Figure 2.7), vertical profiles of velocity components [u* and v*, as in Figure 2.8 (a)], velocity vectors [as in Figure 2.8 (b)], water-surface mapping [as in Figure 2.9 (a)], and turbulent kinetic energy (k) distribution [as in Figure 2.9 (b)]. The graphs are all related to one flow discharge ratio scenario, which is defined as $q^* = Q_m$ (main channel discharge) / Q_t (total outflow) and equals to 0,25 in this case, though seven different scenarios were studied. The coordinates are nondimensionalised when divided by W, the width of the flume. The experimental results of Weber *et al.* (2001) are better exposed on Huang (2000), where the data is obtained from.

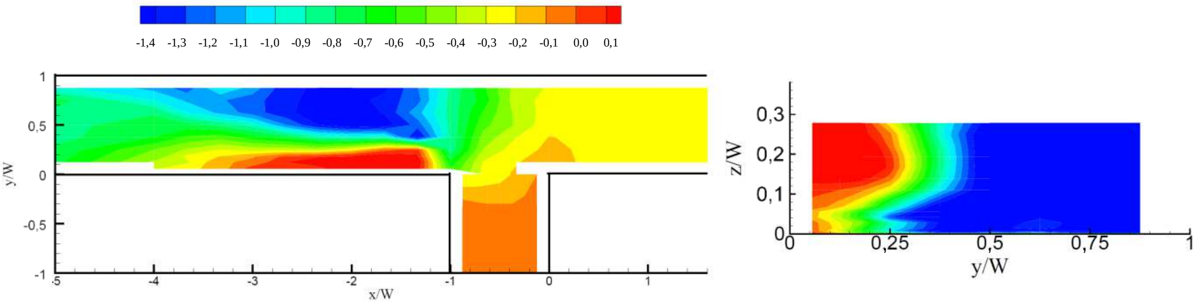

(a) (b)

Figure 2.7: Experimental u* velocity distribution in (a) plan view (z/W = 0,278) and (b) cross-section (x/W = -2) (Huang, 2000)

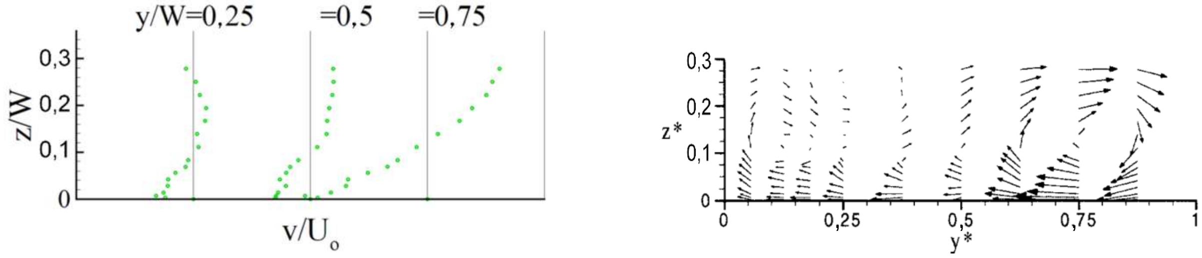

(a) (b)

Figure 2.8: (a) Experimental vertical profile of transversal velocities (x/W = -2) [adapted from Huang (2000)] and (b) cross-section of experimental velocity vectors (x/W = -2) (Weber et al., 2001)

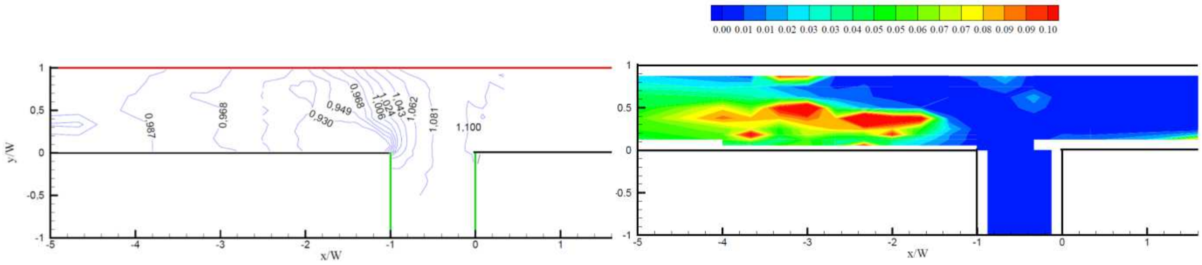

(a) (b)

Figure 2.9: Exp. (a) water-surface mapping and (b) k distribution (z/W = 0,278) (Huang, 2000)

From these and other graphs of different regions and for different flow scenarios, it can be said that a complete description of the flow structure in the vicinity of a junction is possible to be made. The main characteristics of the flow patterns are:

- The separation zone (reddish region in Figure 2.7) is generated in the left wall, just downstream the junction. It is constituted of a recirculation zone in the middle, where positive velocities (upstream motion) are found, surrounded by an outer layer of very low velocities that makes the separation from the streamwise flow.
- The largest longitudinal velocities (bluish region in Figure 2.7) occur just downstream of the junction at x/W = -2, in the main channel flow region contracted by the zone of separation.
- As q* decreases, i.e. as less discharge enters from the main channel, the separation zone increases in width and length, causing a higher contraction of the main channel and, therefore, higher velocities in this contracted region. This trend continues up to a certain limit when so much flow enters from the lateral branch that the reflection of the lateral flow off the opposite wall collapses the downstream end of the separation zone, effectively shortening it. In those experiments only q* = 0,083 displayed this feature, so scenario q* = 0,250 presented the largest separation zone from the seven.

- The flow patterns close to the bottom are different from those close to free-surface. The separation zone is larger near the surface, both in width and length, with more recirculation inside it.
- Though not properly represented in the former figures, a stagnation point is present around the upstream corner of the channel junction, where the velocities are very small.
- A clockwise helicoidal current is created along the downstream channel, which can be noticed in Figure 2.8. This is generated due to the shock of the side channel flow against the junction-opposite wall that reflects the flow downwards, since the higher velocities are in the surface, and downstream, by the oncoming main channel water. On its return, when the flow is closer to the bed and approaching the downstream channel left side wall, the flow is also deflected upward into the zone of separation. Eventually, the entire channel is engulfed in a large clockwise secondary current that is diminished on its way downstream.
- For all flow conditions the water-surface [shown in Figure 2.9 (a)] generally displays a drawdown longitude profile as the flow enters the contracted region and then exhibits a depth increase as the flow expands to the entire channel width downstream of the separation zone. For scenario $q^* = 0{,}250$, the highest depth upstream in the main channel is $1{,}104H_o$ (H_o = tailwater depth = 0,296 m) or 31 mm higher than H_o, while the lowest depth at the contracted region is $0{,}916H_o$, or 25 mm lower than H_o.

From the information above, it is clear that the critical reach to be modeled is located in the downstream channel in between x/W = -1 to -4, where the flow is more three-dimensional, intense and turbulent, consisting the focus on any CFD model validation.

So, with these experimental results in hand, Huang *et al.* (2002) developed and validated a confluence CFD model that discretizes the governing equations by the finite-volume method, appling the standard k-ε turbulence model for closure and models the free-surface by a sort of mesh-regeneration method, which allows the grid to be molded according to the calculated water-surface during the iterations until reach convergence. This method claims to be able to capture the water-surface behavior without the need of performing the costly Volume of Fluids method, which deals with a multiphase flow (water and air). The research also carried out an investigation on the effect of the junction angle on the flow characteristics. The following figures present a few of the extensive comparisons between the physical and the numerical model for a 90° confluence, better exposed in Huang (2000). Here, only the results of the scenario q* = 0,25 are presented.

Figure 2.10 shows that this mesh regeneration was able to roughly reproduce the water surface, though underestimating both the elevations at the upstream channel and the depression around separation zone, what becomes something not distant from a constant level flow.

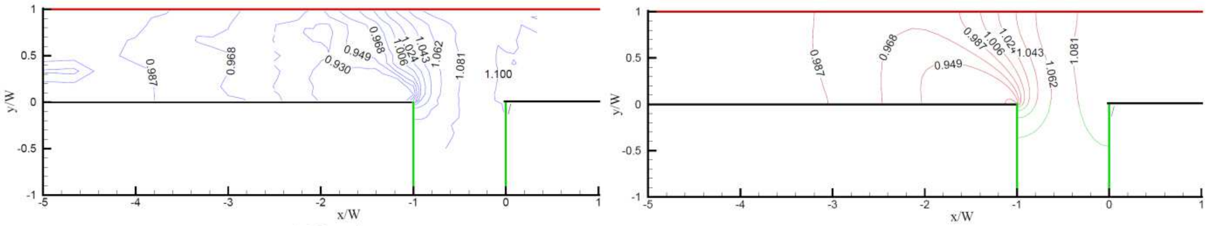

(a) Experiment

(b) Calculation

Figure 2.10: Plan view comparison of experimental and calculated free-surface mapping from Huang (2000)

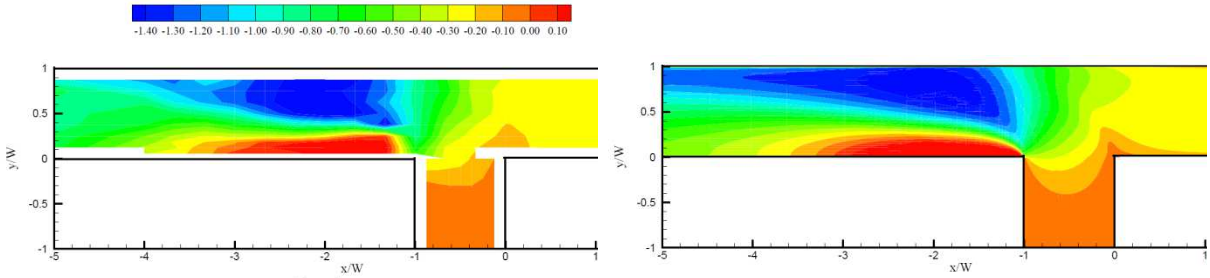

Experiment

Calculation

Figure 2.11: Plan view comparison of experimental and calculated u* velocity distribution at z/W = 0,278 from Huang (2000)

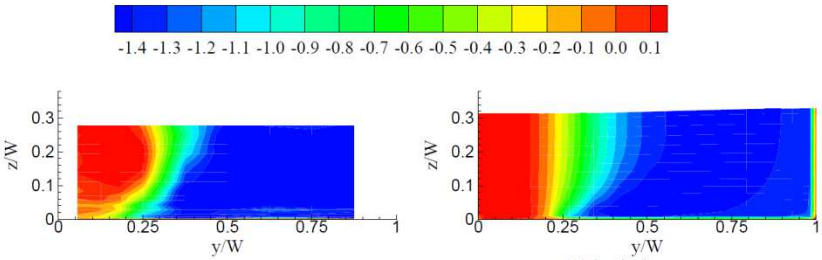

Experiment

Calculation

Figure 2.12: Cross-sectional comparison of experimental and calculated u* velocity distribution at x/W = -1,67 from Huang (2000)

Most of the important hydrodynamic characteristics of the junction flow was reproduced by the model, specially the streamwise velocities, as it can be seen from Figure 2.11 to Figure 2.13. The model predicted well the size of the recircularion zone at the top, though overestimating its size at the bottom (Figure 2.12).

Vertical velocity profiles confirm that streamwise velocities were accuratly captured in most of the confluence. Nevertheless, some mispredictions again can be found, for example at cross-section x/W = -2 [inside the critical reach, Figure 2.13 (a)] and, in a smaller degree, at x/W = -6 [farther downstream, Figure 2.13 (b)].

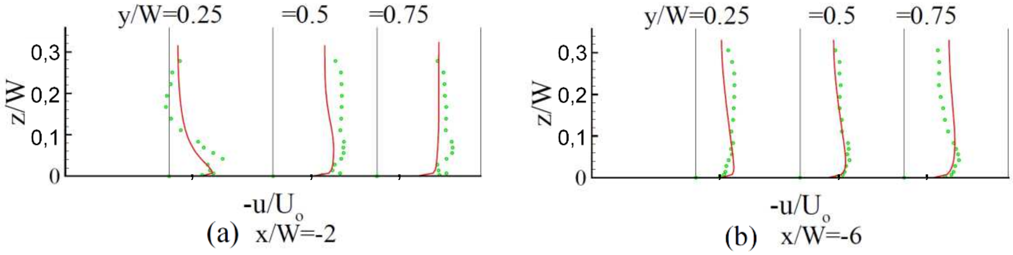

Figure 2.13: Comparison of experimental and calculated vertical profiles of streamwise velocity from Huang (2000)

Analysing the vertical profiles of transverse velocities, it can be realised that the model is not as effective in capturing the transversal motion in details. In Figure 2.14 (a), for example, it is also noted that the reflection of the side channel flow against the right-wall of the main channel is quite underpredicted. Consequently, at x/W = -6 the modeled clockwise helicoidal is nearly over, when, in reality, it still has some effects in the transverse velocities [Figure 2.14 (b)]. In Figure 2.15, plan views of velocity vectors confirm that the model really has some difficulties in replicating the reflection on the right-wall, since the measured vectors point towards the wall at z/W = 0,278 and off the wall at z/W = 0,014, when the numerical results give an approximate straight track alongside the wall.

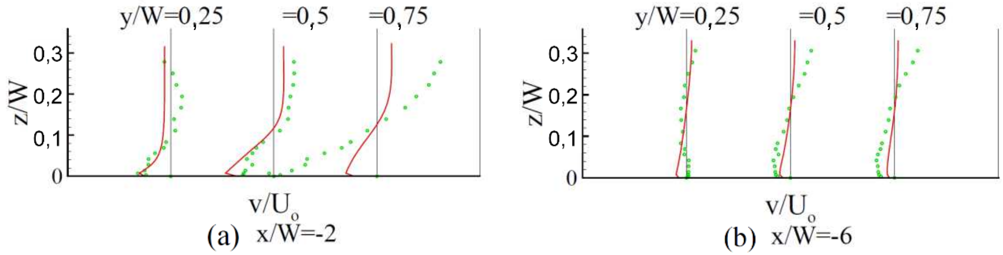

Figure 2.14: Comparison of experimental and calculated vertical profiles of transverse velocity from Huang (2000)

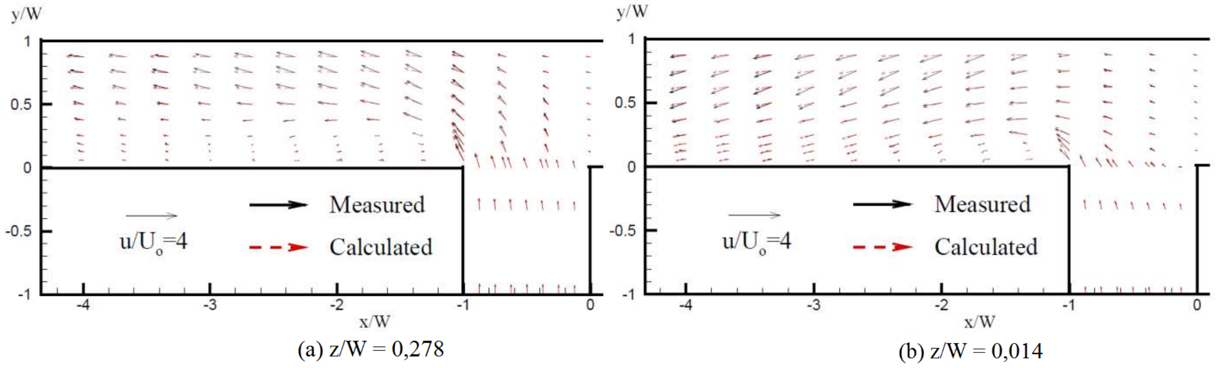

(a) z/W = 0,278

(b) z/W = 0,014

Figure 2.15: Plan view comparison of experimental and calculated velocity vectors at two different elevations from Huang (2000)

Comparison of velocity vectors is made by Huang (2000) confirming that the model underestimates the strength of the secondary flows. Finally, numerical turbulent kinetic energy, k, is evaluated and also found to be underpredicted, specially in the surroundings of the separatio zone where there is a high production of k.

Huang *et al.* (2002) conclude suggesting the use of a higher-order turbulence models to improve prediction, what motivates the use of the LES model in this research.

The second cited research that assessed confluence CFD modeling on confluences was Dordevic (2012), who analyzed three study cases: the experimental data of Weber *et al.* (2001); another experimental data, a 30° confluence of Biron *et al.* (1996); and the author’s field data on Danube River in Belgrade, with the increasing complexity of the confluence morphology. The software SSIIM2 was performed, also based on the finite-volume method, appling the standard k-ε turbulence model for closure but treating the free-surface as a rigid lid, which considers the surface as constant and non-frictional.

The analysis made by Dordevic (2012) focused on the comparison of the measured and calculated velocity profiles. Very few graphs were presented on the validation of the prismatic 90° confluence. In this case, only one scenario of flow ratio was studied, q* = 0,583.

Figure 2.16 shows velocity vector fields and traces the separation zone at some elevation, unfortunately not mentioned, where the width of this zone was captured well but its length was underpredicted in about 20%.

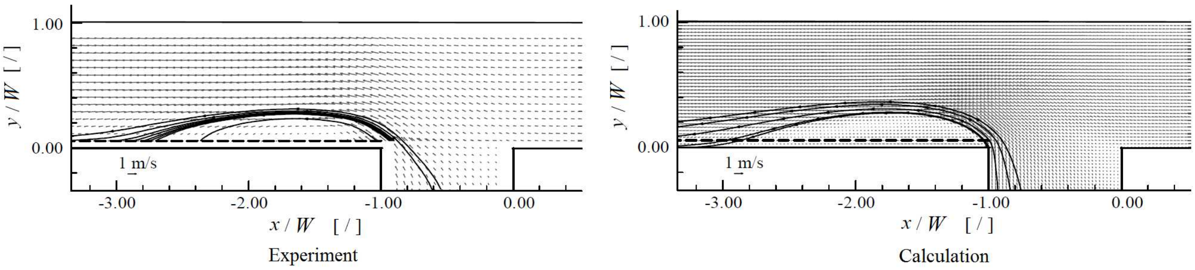

Figure 2.16: Comparison of measured and calculated velocity vector fields from Dordevic (2012)

In Figure 2.17, it can be seen the good approximation of the measured and calculated streamwise velocity distributions. However the velocities magnitudes were underpredicted, especially at the contracted zone, as shown by profiles y/W = 0,375 and 0,875 at cross-section x/W = -1,67. Another weakness is that the model fails to describe circulation within the separation zone, as it is concluded from the profile inside the separation zone (y/W = 0.056 at x/W = -1,67). Figure 2.18 brings the transverse velocity profiles and shows that this component, of smaller magnitudes, was appropriately reproduced by the model.

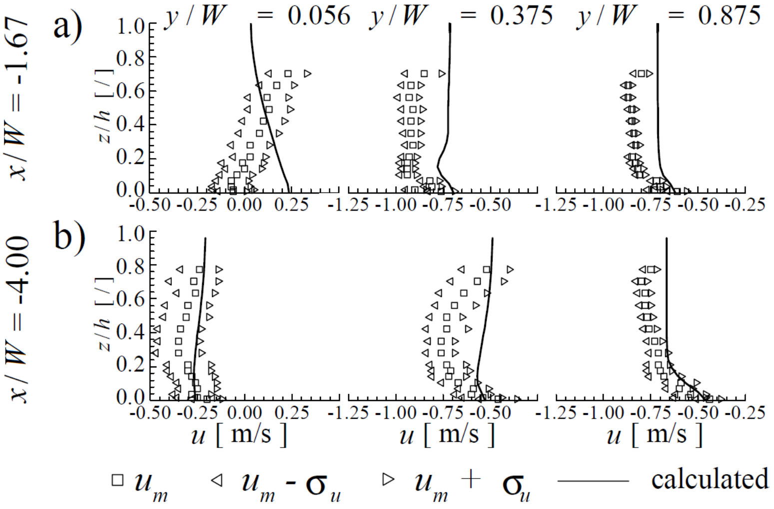

Figure 2.17: Comparison of experimental and calculated vertical profiles of streamwise velocity from Dordevic (2012)

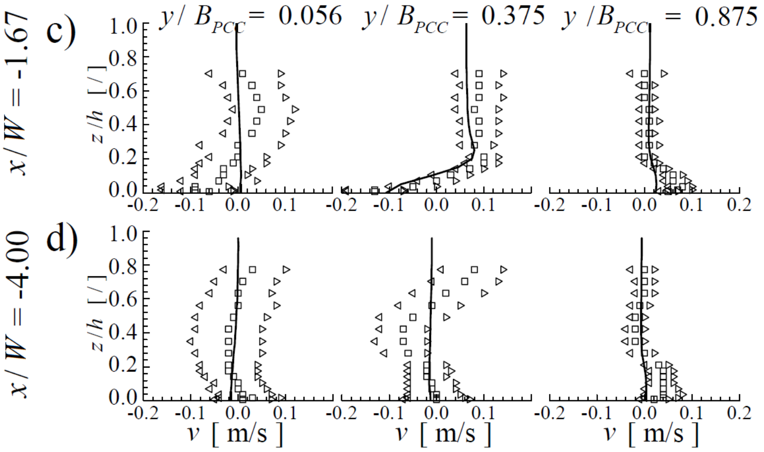

Figure 2.18: Comparison of experimental and calculated vertical profiles of transverse velocity from Dordevic (2012)

It is interesting to note in Figure 2.17 and Figure 2.18 that the measurements' values have some significant deviation, which should be taken into account when judging the accuracy of the numerical model results. Therefore, from the information provided, it can be concluded that the model was able to reproduce satisfactorily the main flow features, even by adopting ffgeometry's top boundary (rigid lid) was located, but apparentely it was adopted higher than it should be, what could be one of the reasons of the underestimated streawise velocities.

Ramamurthy *et al.* (2013) presented an interesting research that, though not on confluences, was very helpful for the work developed here. They set up a model for a channel bend flow, which is highly three-dimensional due to the combined effects of secondary flow and flow separation along the inner bend wall, characteristics also present in confluences. Comparisons with experimental data of flow separation and secondary flow were made from three turbulence models (RNG k-ε, RSM and LES), and four water-surface treatments [Rigid Lid (RL) assumption, Porosity (POR) concept, Height Of Liquids (HOL) concept, and Volume Of Fluids (VOF) method]. Phoenics and Fluent were the softwares used for calculations. Table 2.2 summarizes some important bend flow characteristics measured and calculated for all scenarios.

It is clear that the VOF was the best free-surface treatment method. Its great performance can also be noticed by comparing experimental and numerical plan views of horizontal velocities in Figure 2.19 and Figure 2.20, respectively. Colored contours are related to the horizontal velocity magnitude (named $U_R = \sqrt{u^2 + v^2}$) divided by the inflow average velocity (U_i).

Table 2.2: Measured and predicted bend flow characteristics at z/Z = 0,83 (Ramamurthy *et al.*, 2013)

Source	Grid type	Turbulence model	Water surface	Length of separation	u_{max} (m/s)	u_{min} (m/s)	k_{max} (m^2/s^2)
Experiment				15,0	0,65	-0,09	0,018
Phoenics	BFC	RNG k-ε	POR	8,9	0,62	-0,067	0,005
	BFC	RSM	POR	9,2	0,63	-0,08	0,009
	BFC	RNG k-ε	RL	0,0	0,56	0,000	0,003
	BFC	RNG k-ε	HOL	7,2	0,62	-0,062	0,005
	CAR	RNG k-ε	POR	3,2	0,63	0,053	0,007
Fluent	BFC	RNG k-ε	RL	0,0	0,56	0,000	0,003
	BFC	RSM	RL	0,0	0,58	0,000	0,004
	BFC	LES	RL	12,4	0,61	-0,03	0,048
	BFC	RNG k-ε	VOF	11,2	0,63	-0,08	0,007
	BFC	RSM	VOF	13,4	0,63	-0,09	0,011

Note: BFC = body-fitted coordinate; CAR = Cartesian

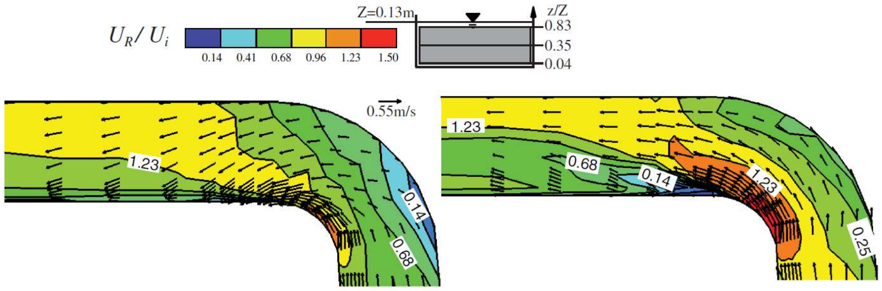

(a) (b)

Figure 2.19: Experimental u-v vectors and U_R/U_i contours at (a) z = 0,05 cm and (b) z = 10,5 cm

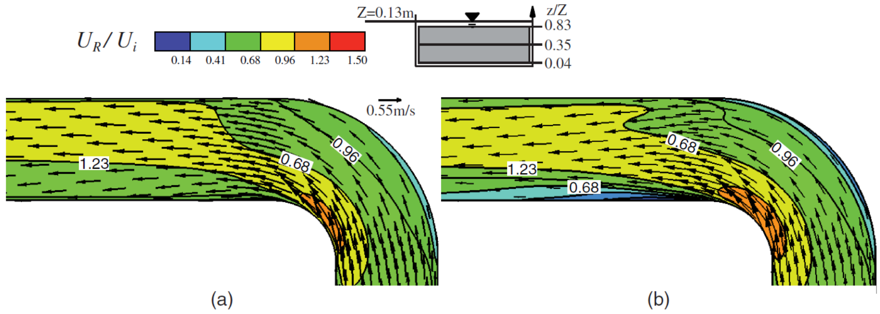

(a) (b)

Figure 2.20: Numerical u-v vectors and U_R/U_i contours for the Fluent model with RSM and VOF at (a) z = 0,05 cm and (b) z = 10,5 cm

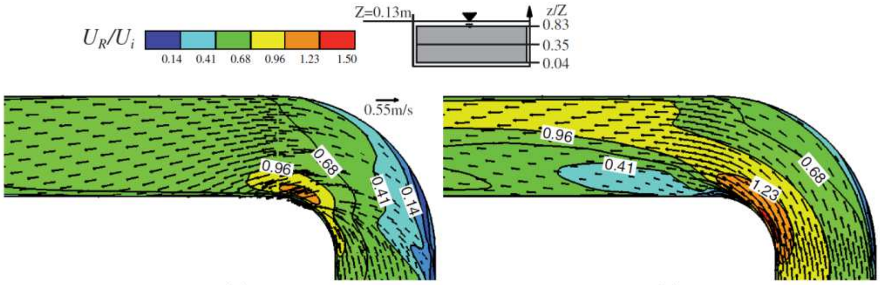

(a) (b)

Figure 2.21: Numerical u-v vectors and U_R/U_i contours for the Fluent model with LES and RL at (a) z = 0,05 cm and (b) z = 10,5 cm

When the results of the three models that assumed a rigid lid are compared, it becomes evident that the LES was the best turbulence model. Nevertheless, some significant imperfections can be noticed in Figure 2.21, as the under predicted velocities closer to the bottom and the underestimation of the separation zone. The latter aspect is attributed by the authors to the lack of water surface variation due to the rigid lid assumption.

From Table 2.2, it can also be noticed that results from the RNG k-ε, a two-equation turbulence model, were not much worse than those delivered by the RSM, a seven-equation turbulence model, what is a good remark since the former demands much less computational efforts.

Based on the studied applications, it is thought to be productive to test OpenFOAM, a free and open-source CFD software, on the simulation of a 90° confluence flow for scenarios of modeling methods different from those already tested in literature, validating them with the experimental data of Weber *et al.* (2001).

2.4.3 OpenFOAM

The OpenFOAM® CFD Toolbox is a free, open source CFD software package. According to OpenFOAM (2014), the software has a large user base across most areas of engineering and science, from both commercial and academic organizations. It has an extensive range of features to solve anything from complex fluid flows involving chemical reactions, turbulence and heat transfer, to solid dynamics and electromagnetics. Its solvers are based on the Finite Volume Method.

One of the biggest advantages of OpenFOAM is its no cost of acquisition, which allows small companies, individual professionals and students to access such a powerful tool without having the considerable cost of purchasing the CFD software or its annual license. The main disadvantage is that, though its package comes with a good post-processor called ParaView, it does not include a user interface that would empower the user to easily pre-process the model, like all commercial CFD packages.

OpenFOAM was developed to be operated exclusively in Linux, which poses an extra difficulty for those not used to it. The basic directory for an OpenFOAM case is structured as shown in Figure 2.22.

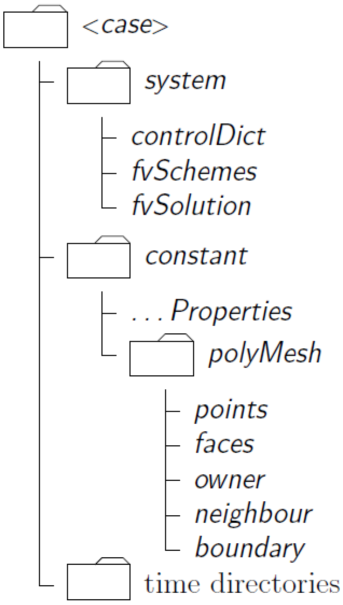

Figure 2.22: OpenFOAM case directory structure (OpenFOAM, 2014)

Into this operating system, for each modeling case, the user has to create a directory of folders and edit standardized files. Domain and mesh have to be edited into the *blockMeshDict* file inside the *polyMesh* folder, which after running the *blockMesh* command generates other geometry files (*points*, *faces*…). The turbulence model chosen is detailed into files inside the folder *Properties*. Boundary and Initial conditions are set into *time directories* in files inside the sub-directory 0, since the case is set up to start at time t = 0. Control parameters are defined into the *controlDict* file inside the *system* directory. The numerical schemes are specified into the files *fvSchemes* and *fvSolution*, also in the *system* directory. After running the case, time directories (as many as the time steps defined into *controlDict* file) will be automatically created with the modeling results.

The good side of not being able to "push buttons" like in the commercial software is that the user is forced to go deep into the modeling features and numerical methods, which may qualify him/her as a mindful and sensible user.

OpenFOAM has been widely used in hydraulic simulations, even in very complex cases. Nevertheless, unfortunately, in literature there are very few researches on OpenFOAM modeling of open-channel flows and maybe none on modeling of confluences.

All this aspects challenge the new OpenFOAM user, especially those pioneering in open-channel modeling, to thrive in a learning curve rather steep but, hopefully, also rewarding.

3 METHODOLOGY

3.1 Study case

In this chapter, the experimental details of the physical model study of Weber *et al.* (2001), used for the numerical model validation are discussed. They examined a 90°, sharp edged, smooth-wall, open-channel junction for channels of equal width (Figure 3.1). Head tanks on both the main and the side channels supplied the discharge. To ensure a uniform flow entering into the junction branches, perforated plates and 100 mm thick honeycomb were placed at the main and side channel inlets. The steepness of the bottom was zero. The tailwater depth in the downstream channel was controlled by an adjustable tailgate.

The origin of the coordinate system is located at the bed at the upstream corner of the channel junction, as shown in Figure 3.1 and Figure 3.2. All distances were normalized by the channel width, W = 0,914 m (3 ft). The velocity measurements have been nondimensionalized by the outlet average velocity, U_t = 0,628 m/s. The upstream main channel, branch channel and combined tailwater discharges are denoted as Q_m, Q_b and Q_t, respectively. The flow ratio q* is defined as Q_m / Q_t. The total combined flow, Q_t = 0,170 m^3/s, and the tailwater depth, H_o = 0,296 m, were held constant, which results in a subcritical flow of Froude number, F_r = 0,37, and a tailwater average velocity, U_t = 0,628 m/s. Seven different scenarios of flow ratios were tested from q* = 0,083 to 0,917.

Depth measurements were made using a point gauge while velocity measurements were taken using acoustic Doppler velocimeter over a grid defined throughout the junction region. The average velocity and turbulence intensity were calculated from a time series of velocities that were recorded at each location. In addition, a 2D mapping of the water-surface was performed on a 72,2 mm square grid throughout the channel junction.

Figure 3.2 and Figure 3.3 illustrate the locations of all velocity measurements. In the former, it is shown where the cross-sections were located, and in the latter, the vertical profiles are positioned. In total, fifteen to seventeen points measured in each vertical profile (located at heights: 0,2 - 0,6 - 1,2 - 2,5 - 3,8 - 5,1 - 6,3 - 7,6 - 10,1 - 12,6 - 15,2 - 17,8 - 20,3 - 22,8 - 25,3 - 27,9 cm - and 30,4 cm, wherever necessary).

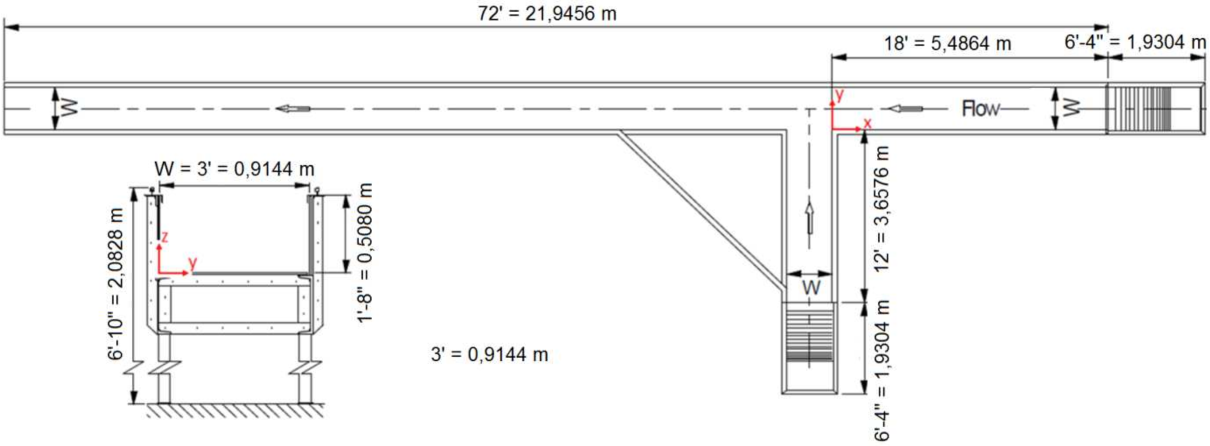

(a) Cross-sectional view (b) Top view

Figure 3.1: Experimental flume layout (adapted from Weber *et al.*, 2001)

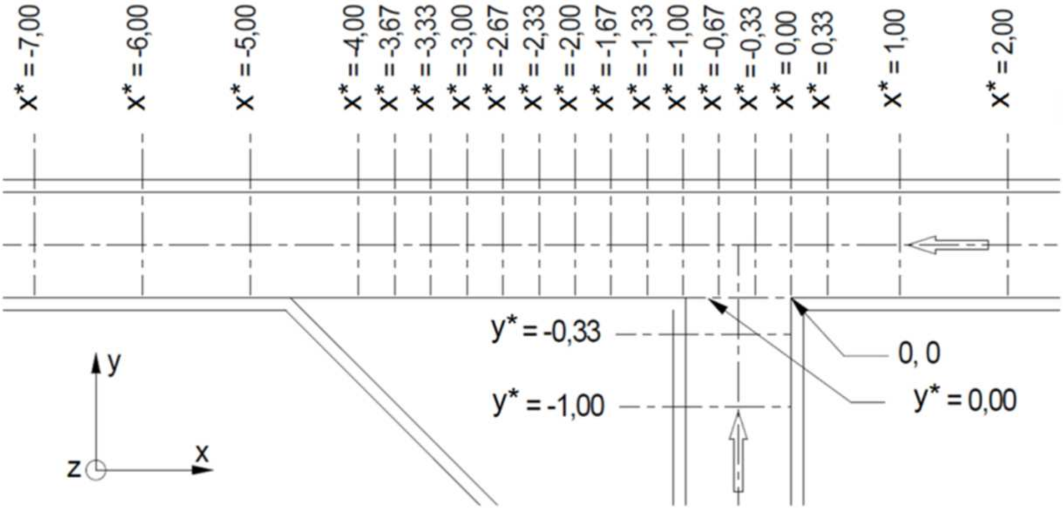

Figure 3.2: Cross-section location for data collection (Weber *et al.*, 2001)

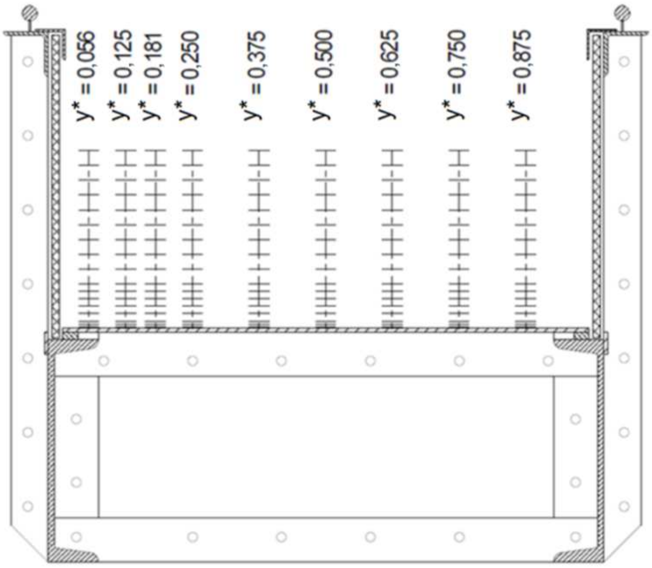

Figure 3.3: Data collection locations in each cross-section (Weber *et al.*, 2001)

3.2 Numerical modeling

The numerical modeling was carried out using the software OpenFOAM. Initially, it was necessary some time to get used to the systematic of OpenFOAM, the available tools and how to properly apply them.

An important task was to decide which solver to use. Firstly, it was intended to simulate a multiphase flow, using the *interFoam* solver (for two incompressible, isothermal immiscible fluids using a Volume Of Fluid (VOF) approach), that would capture also the water-surface variation. However, it was not possible to achieve physically correct results with the Volume Of Fluids method, maybe due to some mistakes in the boundary condition settings that were not found in due time. For that reason, it was decided to change the solver to the *pisoFoam* (transient solver for an incompressible single fluid) and treat the surface as a rigid lid, which means that the free-surface would be fixed at a certain depth by adopting a top boundary ("lid") with no friction – the same approach used by, for example, Dordevic (2012).

The turbulence models adopted in this parametric study are the RNG k-ε model, the k-ω model and a LES model.

The finite volume method has many categories of numerical discretization schemes to be selected from a set of options offered by OpenFOAM (OF). These are not discussed deeply in this study. Table 3-1 presents which numerical schemes were adopted.

Table 3-1: Numerical schemes adopted in the finite volume method

Type	OpenFOAM keyword	Adopted
Interpolation scheme	interpolationSchemes	linear
Surface normal gradient scheme	snGradSchemes	corrected
Gradient scheme	gradSchemes	Gauss linear
Divergence scheme	divSchemes	Gauss limited linear
Laplacian schemes	laplacianSchemes	Gauss linear corrected
Time scheme	timeScheme	Euler
Flux calculation	fluxRequired	none

The pre-processing work, described in this chapter, consisted on building an optimal geometry, then setting the appropriate boundary conditions, and finally defining the adequate control parameters. Though there were many intermediate scenarios, only the final settings are described in detail.

3.2.1 Geometry

3.2.1.1 Domain

The lengths and widths of the domain adopted in the numerical model were exactly the same of the flume built by Weber *et al.* (2001) for the physical model study, shown in Figure 3.1. As mentioned previously, the water-surface was treated as a rigid lid. The height of the numerical geometry was, therefore, fixed at the tailwater depth, H_o = 0,296 m, i.e. 0,031 m lower than the highest physical water level at the main channel inlet, and 0,025 m higher than the lowest water level occurred at the contracted region.

3.2.1.2 Mesh

An optimal mesh refinement was pursued, with the aim of economizing computational costs besides maintaining accuracy. It was pursued firstly by searching for an appropriate mesh grading and, later, by carrying out a mesh independency analysis. These two procedures are treated as follows.

Mesh grading

Constructing the mesh close to boundaries requires further consideration.

Keylock *et al.* (2012) say that close to the free-surface in a LES the size of the grid cell in the vertical direction should not be larger than 1/20 of the channel depth. In this region ideally the shape of the cells should be as close as possible to a cube, apart from the case of a shallow flow dominated by large quasi two-dimensional eddies.

Simulations, especially LES, must have a sufficiently fine mesh to resolve the flow near the channel bed and banks. If wall functions are employed, the case of this research, the first grid point (middle of a cell, in the finite volume method) should be placed in the logarithmic layer. Keylock *et al.* (2012) also say that in practice this first grid point should be at about $30 < y^+ < 300$. On the other hand, Sagaut (2006) mentions that the first point has to be into the range $20 < y^+ < 200$, while Rodi *et al.* (2013) and Versteeg & Malalasekera (2007) indicate that it has to be into the range $30 < y^+ < 500$.

Taking all that in mind, a first coarser mesh was generated, shown in plan view and cross-section in Figure 3.4 and Figure 3.5, respectively.

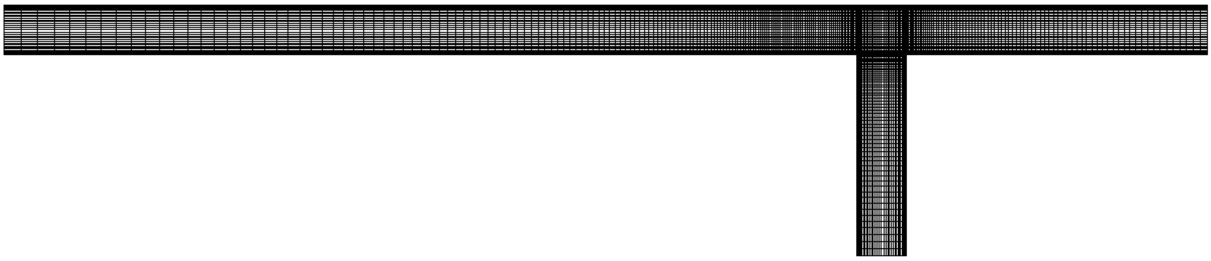

Figure 3.4: Plan view of coarser mesh

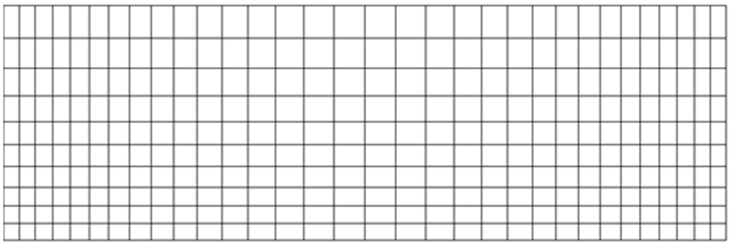

Figure 3.5: Cross-section of coarser mesh

It can be noticed in Figure 3.4 that in the more upstream and downstream parts of the channels, the length of the cells are larger than in the confluence surroundings. This choice could be justified by the fact that in this regions the streamwise velocity gradients are not high and, therefore, a fine grid is not necessary. On the other way, in the reach of the separation zone a higher refinement was kept.

Mesh independency analysis

The experimental data used in most of the comparison of results was provided in more details by Huang (2000). Figure 3.6 shows in red the locations of the velocity vertical profiles available. In total there are 291 points of measurement available (6 cross-sections, times 3 vertical profiles, times 15 to 17 points in each profile).

After having defined an optimal and appropriate mesh grading, the first scenario (S1) was run with 101.760 cells. Then, a finer mesh (S2) was built by multiplying the number of cells in all directions by 1,5, keeping the same mesh grading, what resulted in 343.440 cells. Finally, a third scenario (S3) was built from the first one, now doubling the number of cells in all directions, totalizing 814.080 cells.

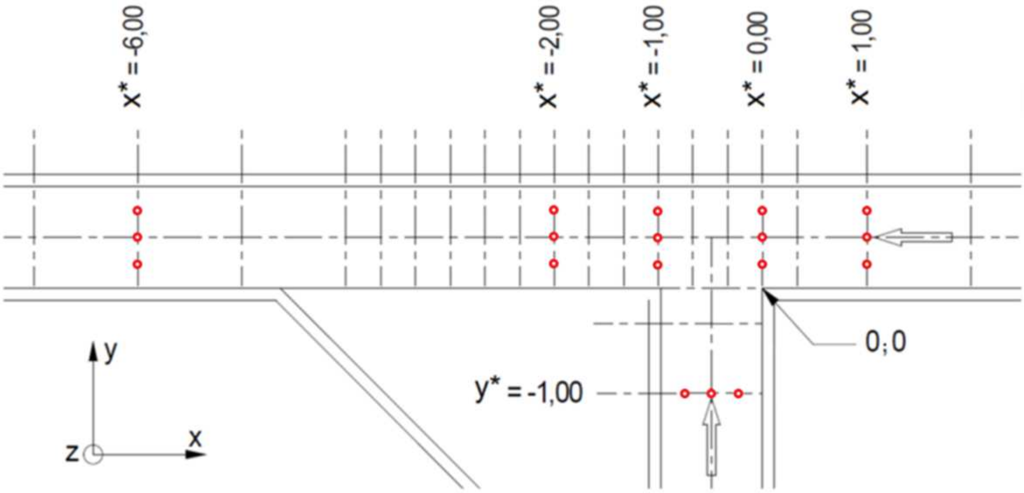

Figure 3.6: Velocity vertical profiles data provided by Huang (2000)

All three scenarios were run using the LES turbulence model and the same parameters, and compared to the experimental results. On this stage, the accuracy was evaluated simply by comparing 90 values of streamwise velocities: 5 in each vertical profiles, located at heights: 1,2; 5,1; 10,1; 17,8; 25,3 cm.

Figure 3.7 presents the dispersion diagram together with an ideal function line, where y = x. It can be seen that the finer the mesh is, the closer the points are to the line. In a perfect model, all points would be above the line and all numerical results would equal the experimental results.

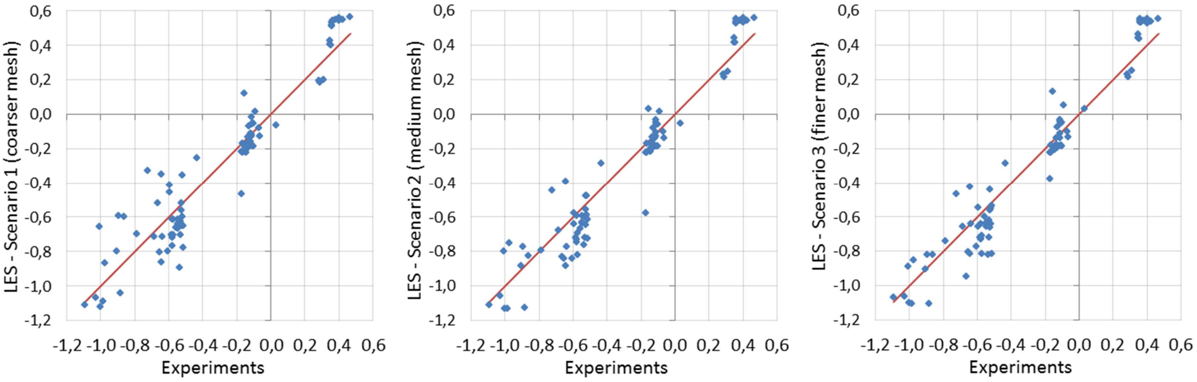

Figure 3.7: Dispersion diagrams of velocities for mesh independency analysis

By calculating the sum of residuals, i.e. the sum of the relative differences between numerical and experimental values, it can be evaluated quantitatively how was the improvement in accuracy. Figure 3.8 plots the sum of residuals in function of the number of cells adopted in each scenario. It can be seen that there was a good improvement in accuracy from S1 to S2. On the second step, from S2 to S3, however, the upgrading was much less significant. It can be estimated that a forth finer scenario would have to adopt an unfeasible amount of cells in order to enhance the quality of the model somehow. Therefore, it was decided to stop the refinement and use S3 mesh (Figure 3.9) in the continuing of this research (parametric study of turbulence models).

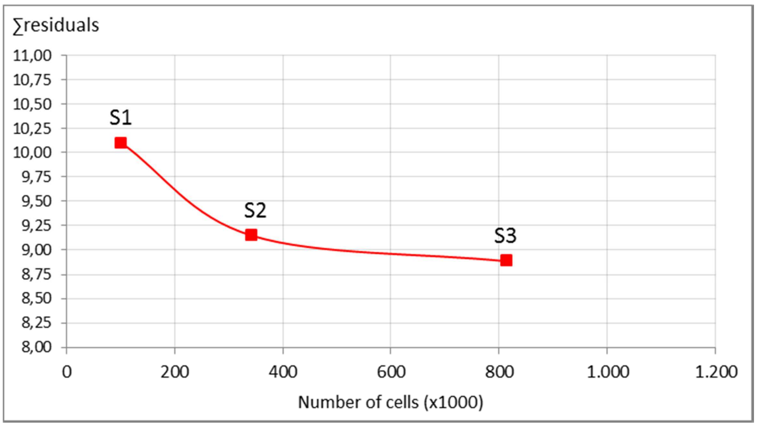

Figure 3.8: Sum of residuals related to the total cells adopted

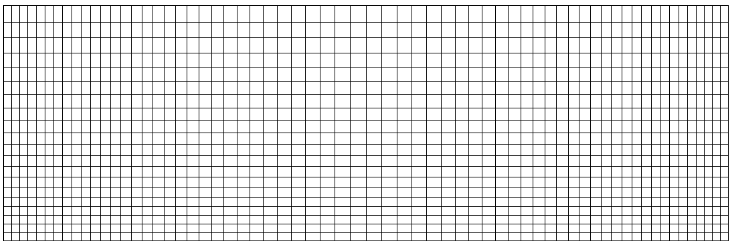

Figure 3.9: Cross-section of the finer and final mesh

After computations were finished, the OpenFOAM tool *yPlusLES* was applied in order to check values of y^+ (dimensionless distance to the wall). It was found that the average of y^+ values for mesh S1 was 16,7, for S2 was 12,5, and for S3 was 9,8.

3.2.2 Boundary conditions and turbulence models

The confluence domain contains four types of boundaries – the inlets, the outlet, the walls, and the top of the channel (atmosphere) –, each containing one or more faces. The initial and boundary conditions had to be specified for each of these boundary types.

3.2.2.1 Velocity

In this research, the flow ratio $q^* = 0,25$ was chosen to be studied, since it is the most extreme scenario in terms of three-dimensional flow patterns, as discussed in section 2.4.2, and consequently the most challenging scenario to be reproduced in modeling. Accordingly, the flows at the inlets had to be set as 0,0425 m³/s (Q_m) and 0,1275 m³/s (Q_b) for the main channel and the branch channel, respectively. In order to apply that, the velocity at the inlet boundaries were set as a *fixedValue* condition (a constant value, as the name says) with uniform velocity vectors of components (-0,157; 0; 0) and (0; 0,471; 0) m/s for the main channel and the side channel, respectively. Their streamwise velocity components (U_m and V_b) were calculated by the following equations:

$$U_m = \frac{Q_m}{A_c} \qquad and \qquad V_b = \frac{Q_b}{A_c} \tag{3.1}$$

Where:
A_c = cross-sectional area of the (computational) inlets = 0,2707 m²

The choice of setting uniform velocities at the inlets can be justified by the fact that the inlet boundaries of the physical model where built with perforated plates, intending to promote the most uniform flow possible, as mentioned in subchapter 3.1. Along the inlet channels, both in the physical and the computational domain, it is expected that the flow is developed to a certain level before reaching the junction. The physical model study data provided by Weber *et al.* (2001) or Huang (2000) does not provide enough information to define how developed the flow is before entering the junction. At this point, due to the short lengths of the inlet channels, it is not expected that the flow reaches a full developed flow.

The outlet face was given a *zeroGradient* boundary condition for velocity, which says that “the normal gradient of velocity is zero”.

A no-slip velocity condition is assumed at the walls by applying a *fixedValue* condition with a uniform value of (0; 0; 0), meaning that the velocity at the wall is zero, according to section 2.3.3.

A *slip* boundary condition for the velocity was adopted at the top, which implies that the normal component is *fixedValue* zero, and tangential components are *zeroGradient*.

A command called *setFields* was used to define the initial velocities into the domain. For the whole main channel cells, the velocity of (-0,157; 0; 0) was set, while for the branch channel cells, before the junction, it was (0; 0,471; 0). This tool is optional and it was useful to improve the stabilization of the flow to its uniform state, controlled by the boundary conditions, after some simulation time.

3.2.2.2 Pressure

The pressure was set as *zeroGradient* at all boundaries of the domain except at the outlet, where the pressure was considered as *fixedValue* with zero value. The initial pressure at all boundaries was defined as zero.

3.2.2.3 Turbulent kinetic energy

The turbulent kinetic energy at the inlets was determined by a boundary condition called *turbulentIntensityKineticEnergyInlet* in OpenFOAM. It is based on user-supplied turbulence intensity, defined as a fraction of the mean velocity:

$$k_p = 1{,}5(I|\boldsymbol{U}|)^2 \tag{3.2}$$

Where:
k_p = turbulent kinetic energy at the patch
I = turbulence intensity = **u’/U**
|**U**| = magnitude of the velocity vector

A turbulence intensity of 10% was adopted in order to represent the turbulence generated by the effect of the perforated plates at the inlets.

A *zeroGradient* boundary condition for k was assumed at the outlet.

At the walls a boundary condition called *kqRWallFunction* provides a suitable condition for k fields for the case of high Reynolds number flow using wall functions. It is a simple wrapper around the *zeroGradient* condition.

At the top face, a *zeroGradient* condition for k was adopted.

The initial turbulent kinetic energy at all boundaries was defined as 0,015 kg.m^2/s^2. This value was found by inserting |**U**| of 1 m/s and I of 10% into equation 3.2.

3.2.2.4 SGS kinematic viscosity (for LES)

The last parameter to have its boundary conditions defined in the LES model is the sub-grid scale kinematic viscosity, ν_{SGS} or nuSGS (OpenFOAM terminology).

At the walls a boundary condition called *nutkWallFunction* provides a turbulent kinematic viscosity condition when using wall functions, based on turbulence kinetic energy. At all other boundaries a *zeroGradient* condition was adopted. The initial ν_{SGS} at all boundaries was defined as zero.

3.2.2.5 Turbulent viscosity (for RNG k-ε and k-ω)

In the RNG k-ε and k-ω models, instead, it was necessary to define the boundary conditions for the turbulent viscosity field, ν_t or nut (OpenFOAM terminology).

At the walls a boundary condition also called *nutkWallFunction*, as in the LES model, was applied for ν_t. At all other boundaries, a boundary condition named *calculated* was chosen, which implies that field ν_{SGS} is derived from other fields. The initial ν_t at all boundaries was defined as zero.

3.2.2.6 Rate of dissipation of k, ε (for RNG k-ε)

The last flow parameter to have its boundary conditions defined in the RNG k-ε model is the rate of dissipation, ε or epsilon (OpenFOAM terminology).

At the inlets, the boundary condition for ε was *turbulentMixingLengthDissipationRateInlet*, as called in OpenFOAM. It is based on a specified mixing length. The patch epsilon values, ε_p, are calculated using:

$$\varepsilon_p = \frac{C_\mu^{0,75} k^{1,5}}{l_m} \tag{3.3}$$

Where:

C_μ = model coeficiente, set to 0,09

l_m = mixing length (m)

The mixing length was assumed as the same as a jet, which is accounted as l_m = 0,09L, where L is the half of the jet width, i.e. half of the channel width in this case (equals to 0,457 m). So l_m was supplied as 0,0411 m.

A *zeroGradient* boundary condition for ε was assumed at the outlet.

At the walls a boundary condition called *epsilonWallFunction* provides a turbulence dissipation wall function condition for high Reynolds number in turbulent flow cases. It calculates both ε and G, the turbulence generation field.

At the top face, a *zeroGradient* condition for ε was adopted.

The initial rate of dissipation at all boundaries was defined as 0,0073 m^2/s^3. This value was found by inserting k of 0,015 $kg.m^2/s^2$ into 3.3.

3.2.2.7 Turbulence frequency, ω (for k-ω)

The last flow parameter to have its boundary conditions defined in the k-ω model is the turbulence frequency, ω or omega (OpenFOAM terminology).

At the inlets, the boundary condition for ω was *turbulentMixingLengthFrequencyInlet*, as called in OpenFOAM. It is based on a specified mixing length. The patch omega values, ω_p, are calculated using:

$$\omega_p = \frac{k^{0,5}}{C_\mu^{0,25} l_m} \tag{3.4}$$

The mixing length, l_m, was supplied as 0,0411 m, similarly to what was described in the previous section.

A *zeroGradient* boundary condition for ω was assumed at the outlet.

At the walls a boundary condition called *omegaWallFunction* provides a wall function constraint on turbulence frequency.

At the top face, a *zeroGradient* condition for ω was adopted.

The rate of dissipation at all boundaries was defined as 0,0073 m^2/s^3. This value was found by inserting k of 0,015 m^2/s^2 into 3.3.

3.2.3 Control parameters

The control parameters for running the case in OpenFOAM are set into a file called *controDict*.

As mentioned in section 3.2.1, the more refined mesh, called S3, was used later in the parametric study of turbulence models. All runs in this phase had to be done by the Flemish Supercomputer Center (abbreviated in Dutch as VSC).

A Courant number smaller than one was pursued, even knowing that it was not necessary for achieving temporal accuracy and numerical stability, since the time discretization scheme adopted is implicit. The Courant number, Co, is defined for one cell as:

$$Co = \frac{\delta t|U|}{\delta x} \tag{3.5}$$

Where:
δt = the time step
$|U|$ = the magnitude of the velocity through that cell
δx = the cell size in the direction of the velocity

By estimating the worst case, with the highest |U|, assumed 1,5 m/s (based on experimental data plus a safety gap), and the smallest δx, equal to 0,99 cm (taken from computational mesh), it was possible to choose the appropriate δt, equal to 0,006 s, which maintains Co < 1.

Some virtual probes where inserted at some points into the computational domain and collected the velocity variation through time, allowing the observation of the flow development.

The LES model was run for 77 seconds, before the VSC supercomputer stopped. Figure 3.10 (a) shows the development of longitudinal velocity at point (W; 1/2W; 3/4H_o) located in the main channel before the junction, and (b) shows it at point (-2W; 1/6W; 3/4H_o) into the separation zone.

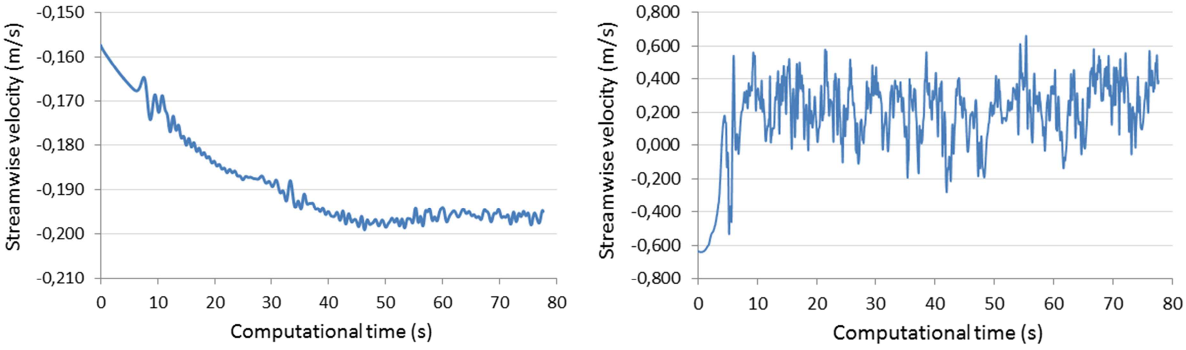

(a) (b)

Figure 3.10: Virtual probes at points (W; 1/2W; 3/4H_o) and (-2W; 1/6W; 3/4H_o) in LES model first simulation

The velocity oscillations captured by the LES model, typical of a turbulent flow, can be seen clearly in the graphs of Figure 3.10, even more accentuated in the separation zone (b), as expected. In order to analyze the results of the LES, it was necessary to obtain the average velocity in a certain time-window after the flow is stabilized (oscillating around a fixed mean value).

Since the probes' graphs did not give the total assurance of flow stabilization, neither provided a time-window long enough to extract mean values, it was decided to run the LES model for a second time, starting from the results of the first run. Figure 3.11 shows the longitudinal velocity oscillations for the second run. This time, the run lasted 62 s and had its values averaged between 30 and 62 s. This time window seems to be sufficient for the flow to reach a stochastic steady-state, since it was checked for some probes in crucial locations that the difference between the average velocity from 30 to 57 s and the average from 30 to 62 s is not significant.

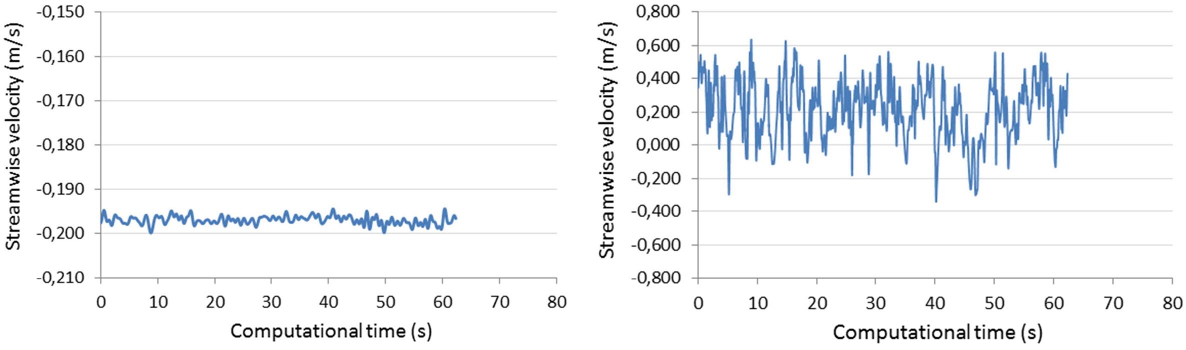

(a) (b)

Figure 3.11: Virtual probes at points (W; 1/2W; 3/4H_o) and (-2W; 1/6W; 3/4H_o) in LES model second simulation

In the RANS equations, since time averaging is intrinsic, there is no velocity oscillation. The simulation needs to be run long enough to have the flow stabilized (no significant velocity variation) dispensing the need to run an extra time window to extract averages. That can be seen in Figure 3.12 and Figure 3.13, which show respectively both RNG k-ε and k-ω models running long to reach flow stabilization. These two-equation turbulence models computations spent each less than 65% of the running time spent per computational time on the LES run.

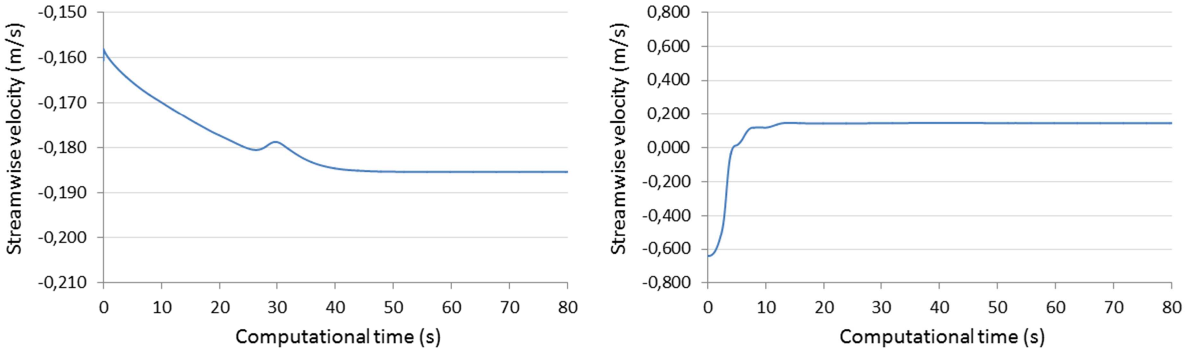

(a) (b)

Figure 3.12: Virtual probes at points (W; 1/2W; 3/4H_o) and (-2W; 1/6W; 3/4H_o) in RNG k-ε model

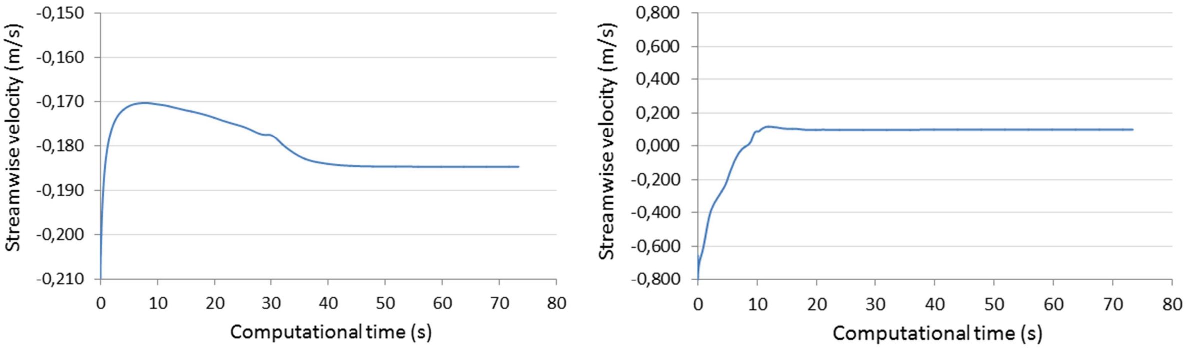

(a) (b)

Figure 3.13: Virtual probes at points (W; 1/2W; 3/4H_o) and (-2W; 1/6W; 3/4H_o) in k-ω model

3.2.4 Validation of numerical model

As mentioned before, the water-surface variation could not be captured. Since a rigid lid approach was adopted, the free-surface was considered fixed at the high of the downstream water level (0,296 m) measured in the experiments. Therefore, the validation of the numerical models here consists basically in comparing velocity distributions and magnitudes (averaged in a time window of 32 seconds, in the case of the LES model) for different components and in several sections and plans.

4 RESULTS AND DISCUSSION

4.1 Velocity vectors

Velocity vectors are useful parameters to start evaluating the behavior of the models' since they enable visualization of the main characteristics of the flow. If eventually something goes wrong with the model the problem can be quickly detected by picturing a plan view of vectors or flow tracks. This evaluation was also made by Huang (2000), Thanh *et al*. (2010), Dordevic (2012) and Ramamurthy *et al.* (2013).

Therefore, the comparison of velocity vectors in a plan view located at z/W = 0,278 is presented in Figure 4.1. It was not possible to elaborate the numerical plots with the same formatting as the numerical plot presented by Huang (2000). Still, it is possible to evaluate the flow track features. Accessing this graph, it becomes clear that the general flow behavior was correctly reproduced by all three turbulence models. It is interesting to see the separation zone well delimited, while on the right side the flow particles are concentrated inside the contracted region. The models, however, fail to describe the reflection of the lateral flow against the right-sided wall of the main channel, as the particles coming from the branch channel, after approximating the main channel wall, flow parallel to downstream channel wall, in agreement with the results of Huang (2000) (Figure 2.15).

In order to make a first comparison, two characteristic angles can be extracted: the angle of entrance of the side channel flow into the main channel; and the angle of the recirculation zone. In Figure 4.2, it is noticed that the two-equation turbulence models present about the same performance, but the LES model was the one that best predicted the flow behavior in this point of view.

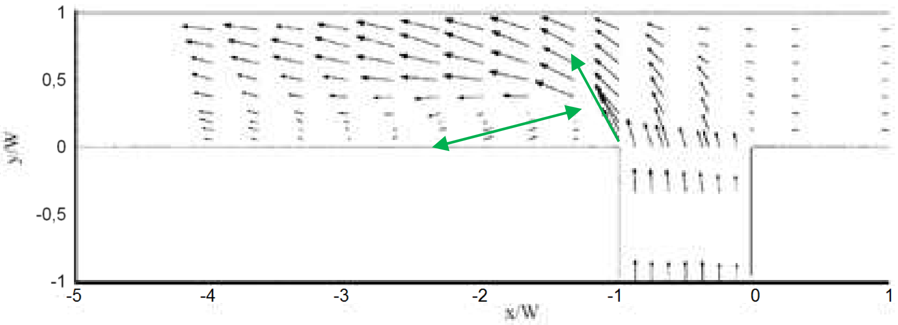

Experiment

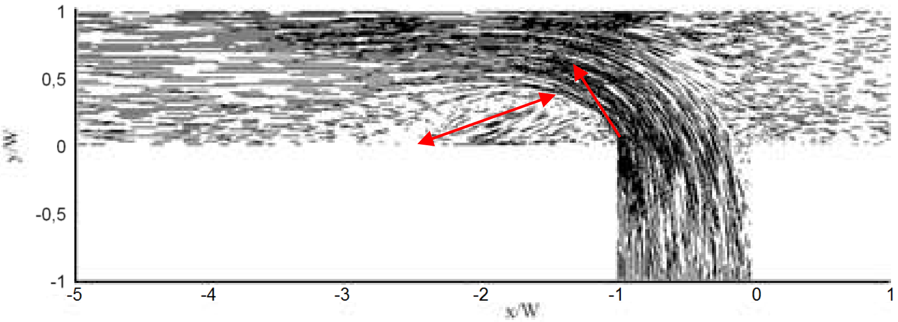

LES

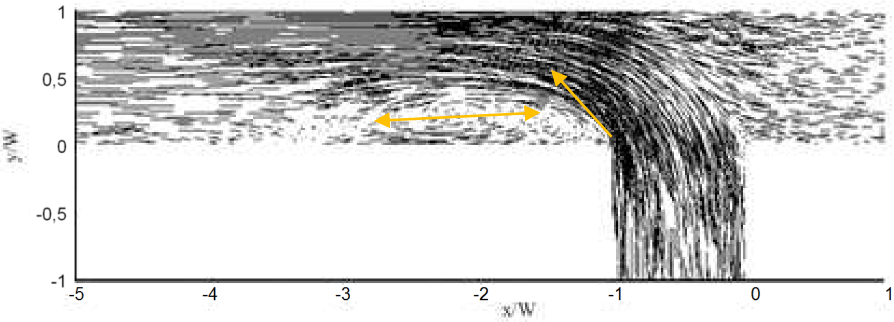

k-ω

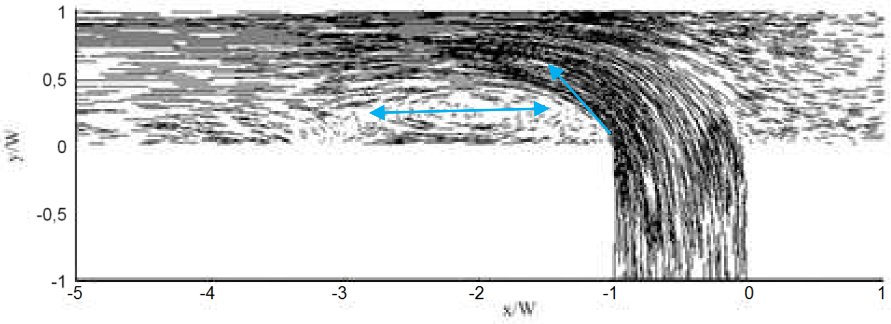

k-ε

Figure 4.1: Plan view of velocity vectors at z/W = 0,278

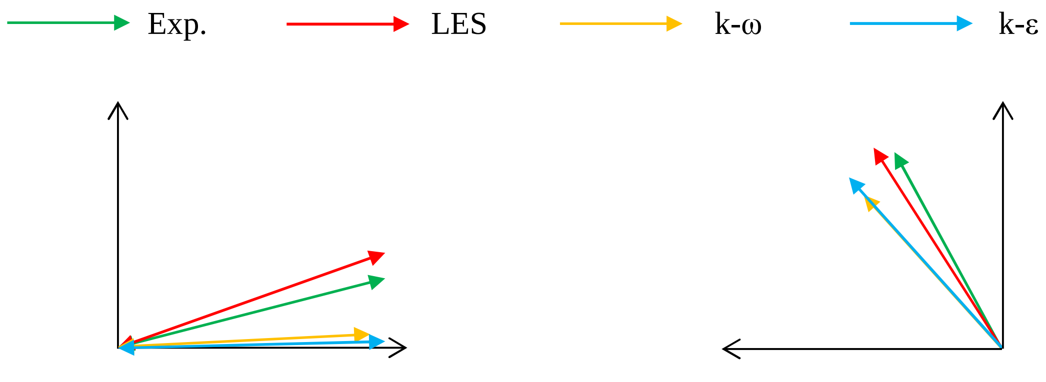

(a) **(b)**

Figure 4.2: Comparison of (a) the angle of recirculation zone and (b) the angle of entrance of side channel flow

4.2 Longitudinal velocities

Velocity component u is defined in the x direction, which is positive pointing upstream. Therefore, u velocity is negative in most of the channel except in the separation zone where the flow is reversed. Since longitudinal velocity is the most significant component in the flow, next sections present comparisons in different forms.

4.2.1 Vertical profiles of longitudinal velocities

Firstly, it is made a comparison similar to what was made in the mesh independency analysis (section 3.2.1.2), by comparing streamwise velocities collected from vertical profiles. However, this time not only 5 but all (15 to 17) points in each vertical profile were used in the comparison, totalizing 291 points of measurement. Figure 4.3 presents the dispersion diagrams comparing the experimental results with those obtained by the three different turbulence models.

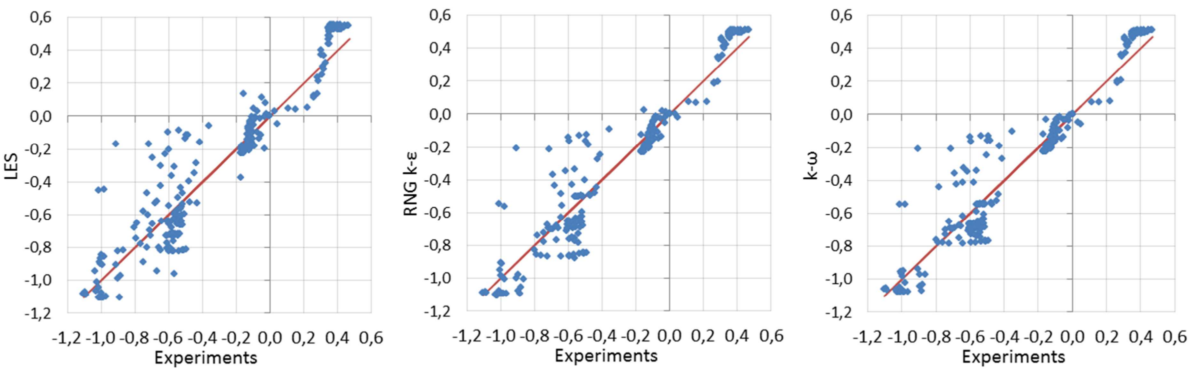

Figure 4.3: Dispersion diagrams of velocities for turbulence models evaluation

As discussed previously in section 3.2.1.2, the line on the graphs is not a regression line, but an ideal line, where x = y, drawn to help visualization of the model accuracy. The sum of residuals were 33,4 for the LES, 28,5 for RNG k-ε and 27,5 for k-ω model.

At first hand, it can be said that the LES model presented less accurate results. Nevertheless, a more in depth analysis should be made in order to evaluate the real accuracy of the turbulence models. In Figure 4.4 to Figure 4.9, the vertical profiles of longitudinal velocities are shown, comparing experimental and numeric data, at 6 cross-sections located as shown in Figure 3.6.

Figure 4.4 and Figure 4.5 display the values obtained at the cross-sections located at the main (x/W = 1) and branch upstream channels (y/W = -1), respectively. The models reproduce the correct shape of the profiles, but always higher than the experimental, what is caused by the 10% difference in water level, a negative impact of applying the rigid lid approach. Figure 2.17 shows that this is in agreement with the findings of Dordevic (2012).

At cross-section x/W = 0 (Figure 4.6), the 10% water level difference is still present, causing again a negative impact. Nevertheless, the profile shape is again well represented by both RNG k-ε and k-ω models, what cannot be said about the LES model.

At cross-section x/W = -1 (Figure 4.7), the water level difference almost disappears. In this case, it can be perceived that the turbulence models better predicted the velocity patterns. The two-equation turbulence models seem to be more accurate.

Figure 4.8 presents the results collected at cross-section x/W = -2, the critical one where the separation zone is the widest and the velocities at the contracted region reach the highest values. Even presenting a peculiar behavior, the experimental left-sided vertical profile (y/W = 0,25), located inside the separation zone, could be surprisingly well captured by the numerical models, especially the RNG k-ε model. The other profiles (y/W = 0,50 and y/W = 0,75), placed in the contracted zone, were also properly represented. It is good to remember that the model of Dordevic (2012) behave poorly around this section for a higher flow ratio scenario [Figure 2.17 (a)] and less three dimensional. It can also be said that the numerical results at this section were even better than those produced by Huang (2000) [Figure 2.13 (a)], who avoided the simplification of the rigid lid approach by applying a sort of mesh-regeneration method to try to reproduce the free-surface.

In Figure 4.9 it can be seen that at cross-section x/W = -6, closer to the outlet, the shape of the experimental profile in the right side differs from the one in the left-side, probably due to helicoidal currents, as explained in section 2.4.2. It seems like the numerical models could not characterize it properly, mainly the LES model, though the left sided profile was very well represented by k-ω model. Huang (2000) also had some difficulties in this section [Figure 2.13 (b)]. At this cross-section and also at the inlets, it is observed that the LES model developed here for some reason underpredicts the velocities near the bottom.

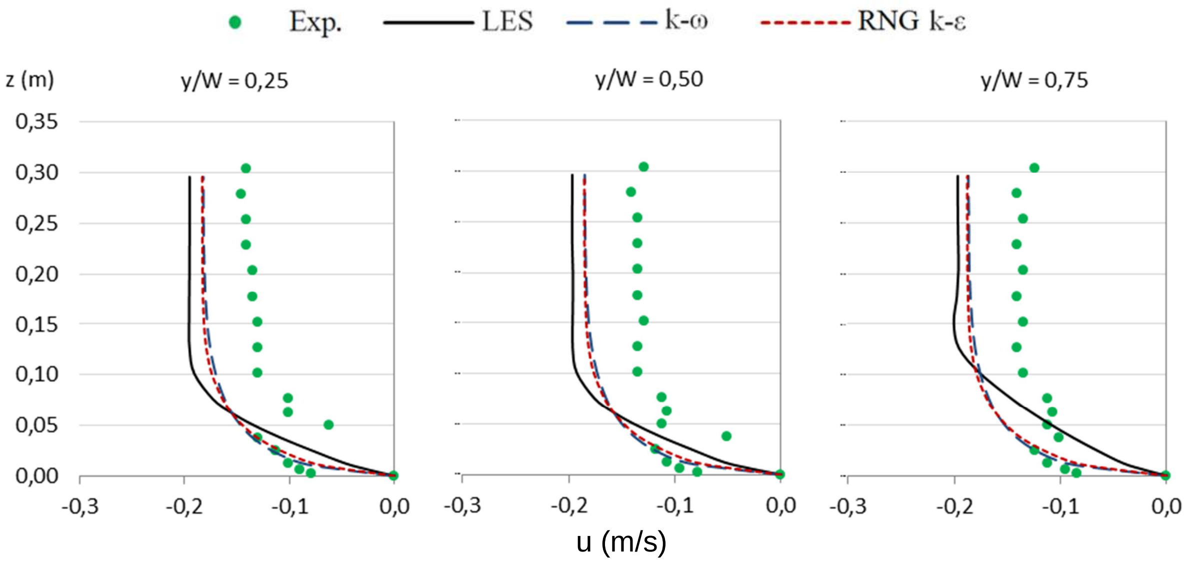

Figure 4.4: Vertical profile of streamwise velocities at x/W = 1

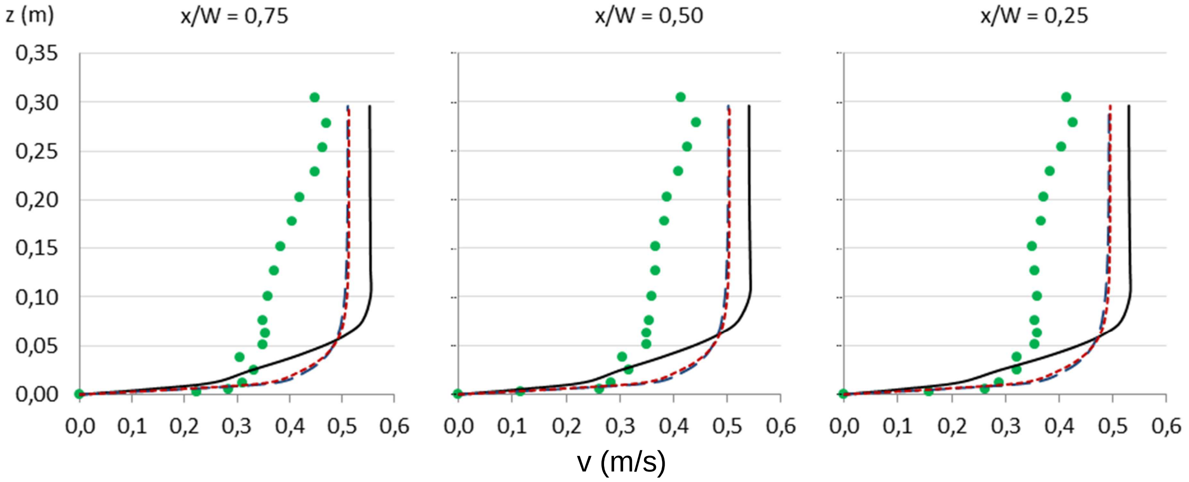

Figure 4.5: Vertical profile of streamwise velocities at y/W = -1

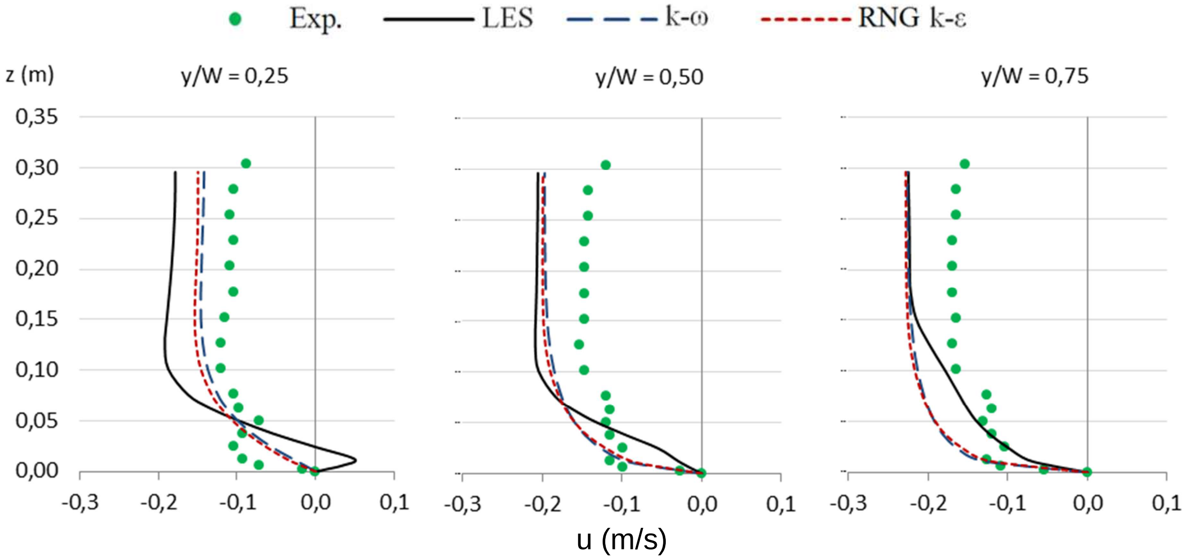

Figure 4.6: Vertical profile of streamwise velocities at x/W = 0

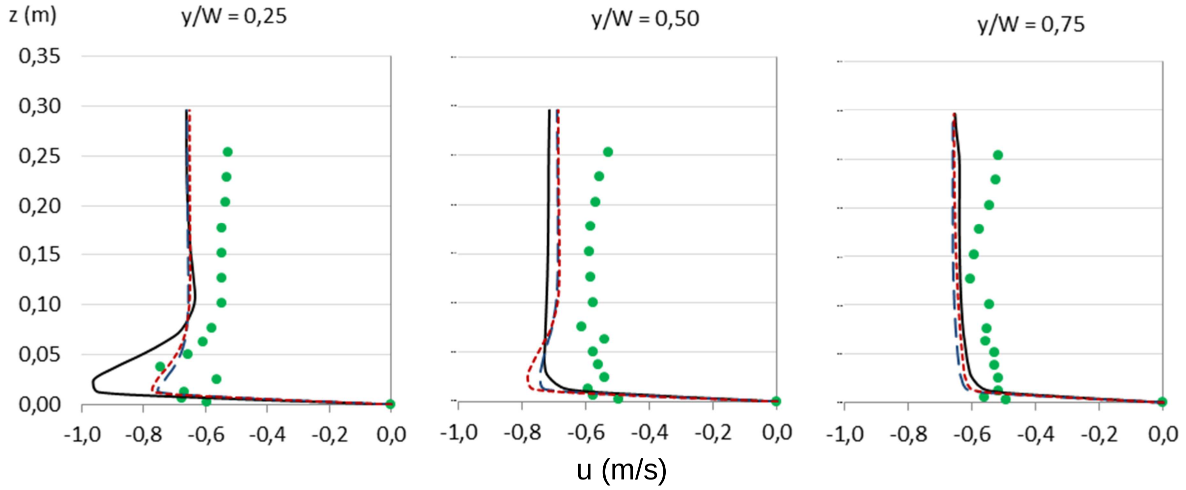

Figure 4.7: Vertical profile of streamwise velocities at x/W = -1

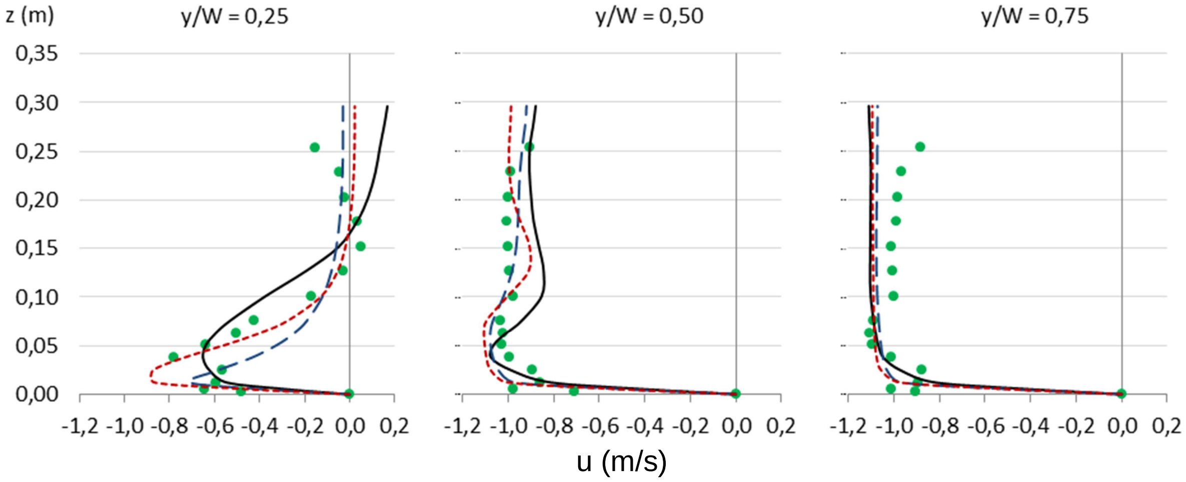

Figure 4.8: Vertical profile of streamwise velocities at x/W = -2

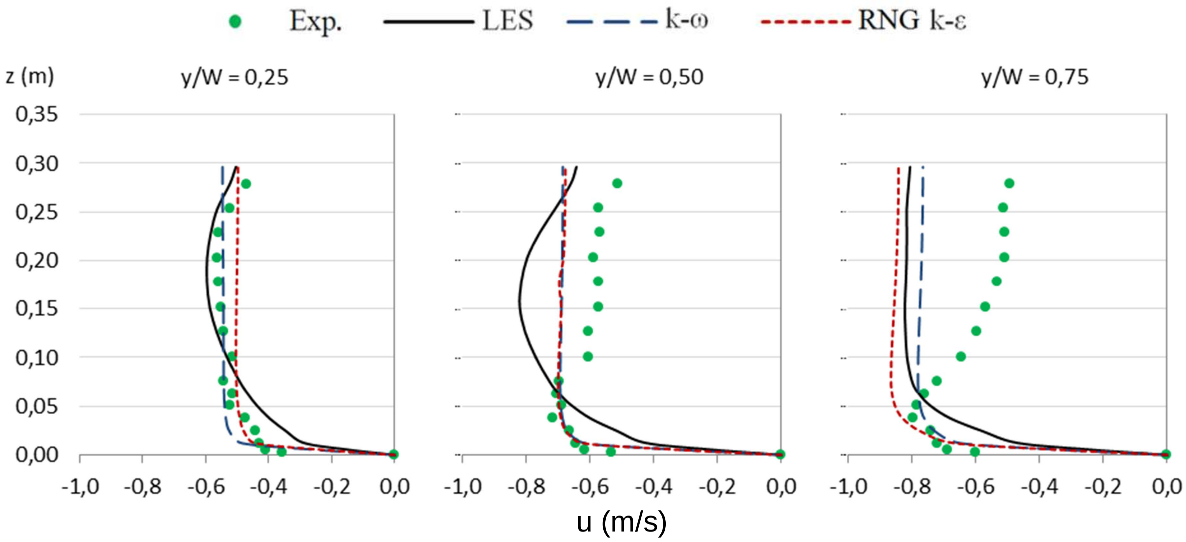

Figure 4.9: Vertical profile of streamwise velocities at x/W = -6

4.2.2 Plan views of u velocity distribution

Figure 4.10 and Figure 4.11 display plan views of the measured and calculated u velocity contours at two water depths, z/W = 0,278 and z/W = 0,014, respectively. These plots present velocities nondimensionalized, divided by the outlet mean velocity, becoming $u^* = u/U_t$. Note that there are blank spots in the experimental plots as measured data are not available in those areas.

The separation zone can be easily identified by the positive values in red, characterizing the reverse flow. A contour dash line was drawn delimitating this region in Figure 4.10 for every model. The lengths and the maximum widths were measured and they are presented in Table 4-1. It is clear that the RNG k-ε model was the one which better reproduced the separation zone, while it was overstretched in the k-ω model and too shortened in the LES model.

Table 4-1: Separation zone dimensions comparison

Model	Length (l/W)	Dif. to Exp.	Max. width (b/W)	Dif. to Exp.
Exp.	2,14	-	0,26	-
RNG k-ε	2,12	-1%	0,28	8%
k-ω	2,48	16%	0,24	-9%
LES	1,71	-20%	0,32	22%

Comparing the plan view of the RNG k-ε model in Figure 4.10 to the one of the model of Huang *et al.* (2002) (Figure 2.11), who applied the k-ε turbulence model, it can be realized that the simplification of the rigid lid approach did not affect the reproduction of the main flow features in the confluence.

The experimental results in Figure 4.11 indicate that near the bottom the recirculation zone tends to disappear. However, all turbulence models overestimated the separation zone at the bottom part. The RNG k-ε model was the one which less did that. The same happened with Huang’s model (Figure 2.12).

Looking at the main channel inlet, it can be observed that the LES model really underpredicts the velocities near the bottom and, consequently, overpredicts those near the water-surface. This is in agreements with the findings of Ramamurthy *et al.* (2013) (Figure 2.21).

Experiments say that the area of higher velocities (in blue) near the bottom is larger than near the surface. The numerical model’s results, however, show the opposite, which is a smaller high velocity area near the bottom, especially on the LES model. This weakness is also present in Huang’s model.

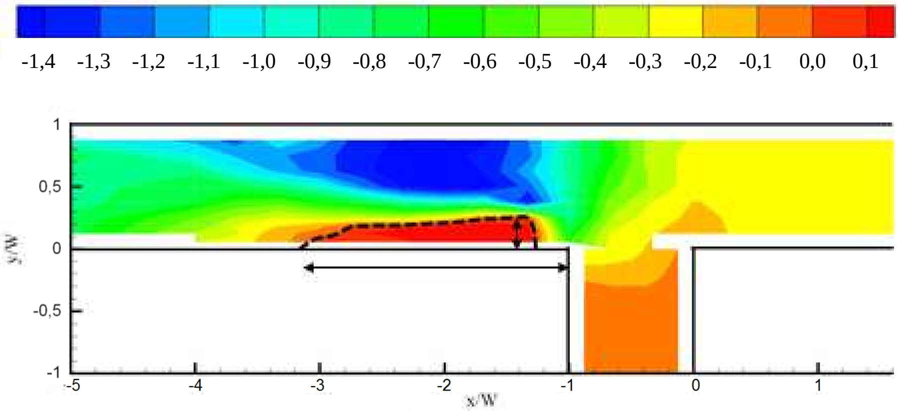

Experiment

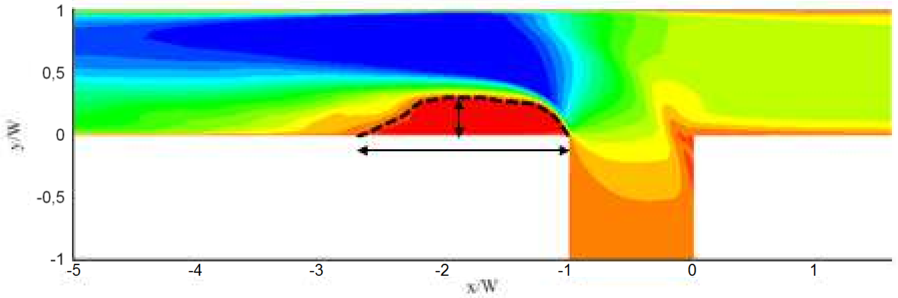

LES

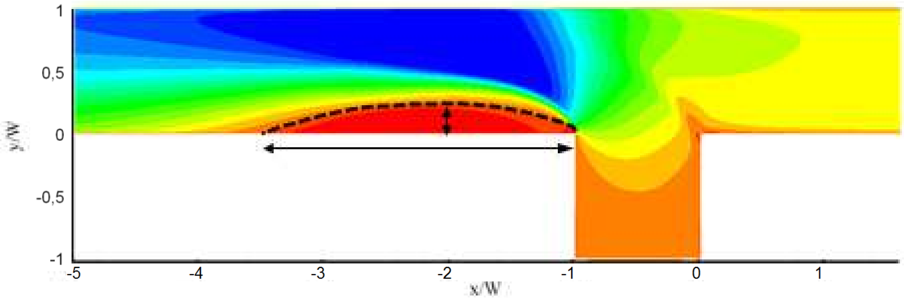

k-ω

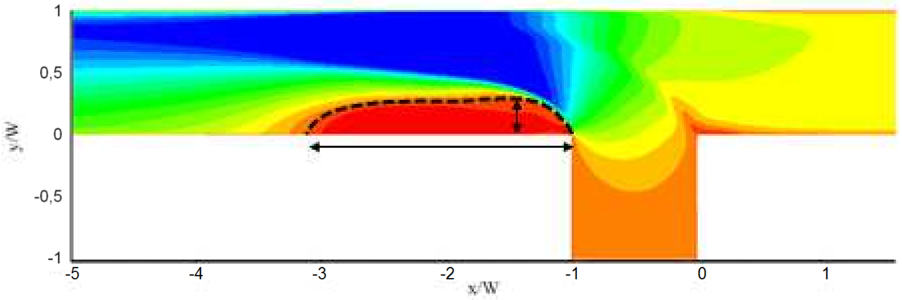

RNG k-ε

Figure 4.10: Plan view of u* velocity distribution at z/W = 0,278

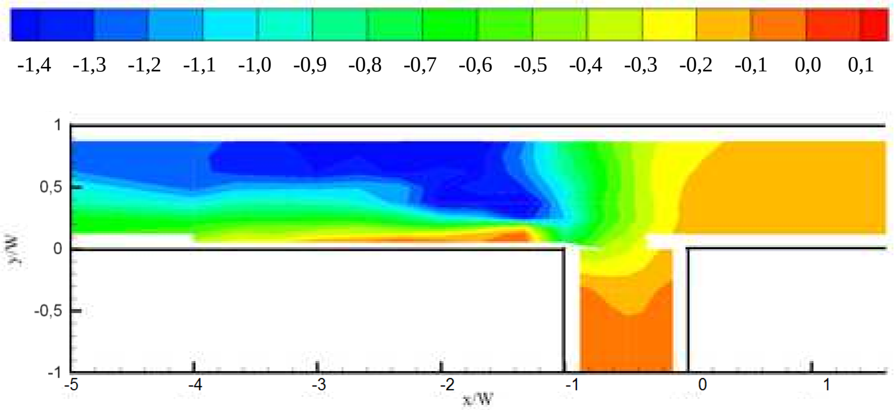

Experiment

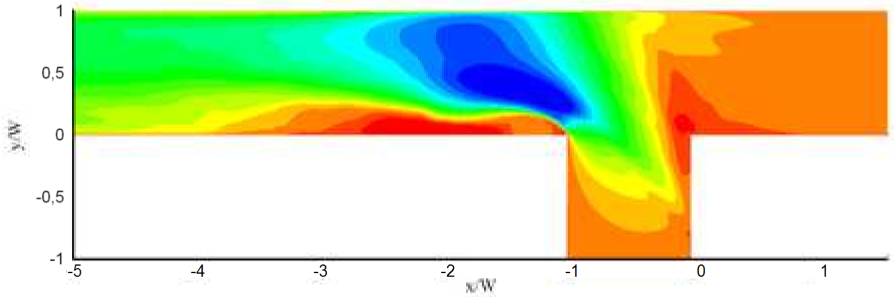

LES

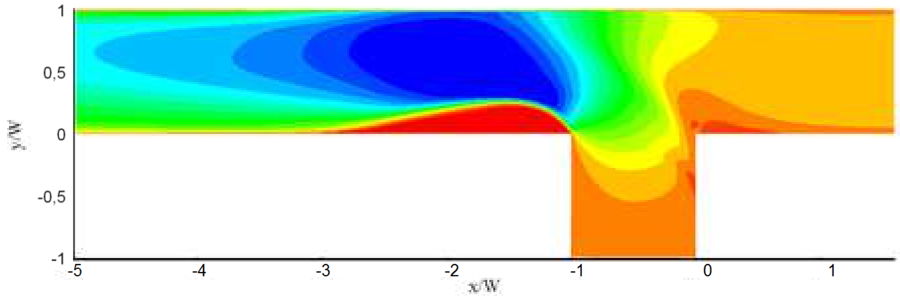

k-ω

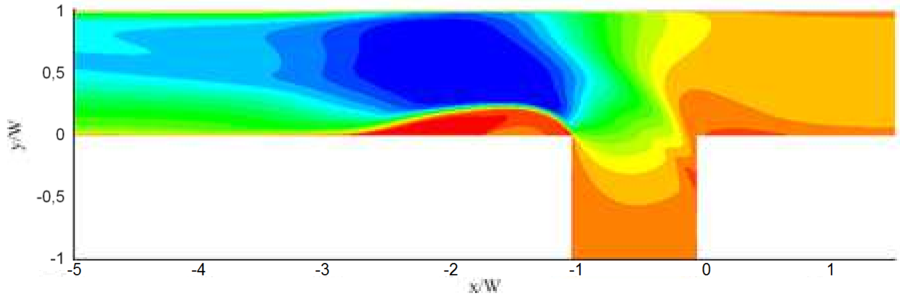

RNG k-ε

Figure 4.11: Plan view of u* velocity distribution at z/W = 0,014

4.2.3 Cross-sections of u velocity distribution

By looking at u velocity distributions in cross-sections (Figure 4.12 to Figure 4.15) other remarks can be made. These plots also present velocities nondimensionalized, divided by the outlet mean velocity, becoming $u^* = u/U_t$. The blank spots in the experimental plots appear again as measured data are not available in those areas.

In cross-section x/W = 0 (Figure 4.12) it is observed that due to the affluence of the branch channel flow just downstream the flow already start migrating to the right side. It is interesting to note here the evidence of a stagnation point in the confluence upstream corner represented by the low (even reversed) velocities in the left side of the main channel cross-sectional plot. Since there is a lack of experimental measurements in this region, it is not possible to determine which numerical model was more accurate.

Cross-section x/W = -1 (Figure 4.13) is aligned with the left wall of the branch channel and where the flow from both channels are added together. This section is in the imminence of the start of the separation zone. The u distribution here was slightly better represented by the k-ω model.

The cross-section where the separation zone is larger is located around x/W = -1,67. Figure 4.14 shows that the results of the numerical models all resemble a lot, though it can be said that the RNG k-ε model provides the best approximation, and even better than that captured by Huang (2000) (Figure 2.12).

Finally, at cross-section x/W = -7 (Figure 4.15), near the outlet, it can be seen the velocities tending to a more uniformly developed flow as the area of higher velocities decreases. Physically this process happens faster than in the numerical models. Though difficult to judge, in this case, it seems like the k-ω is more closely related to reality.

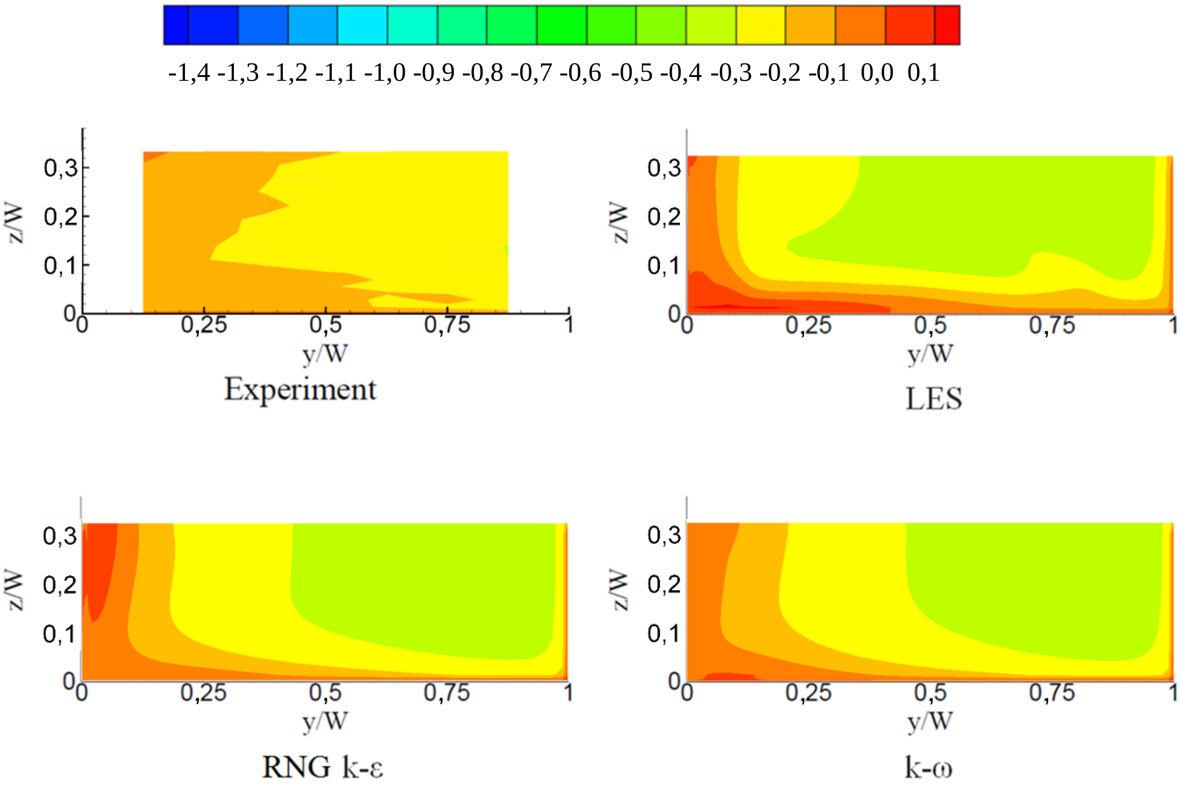

Figure 4.12: Cross-section of u* velocity distribution at x/W = 0

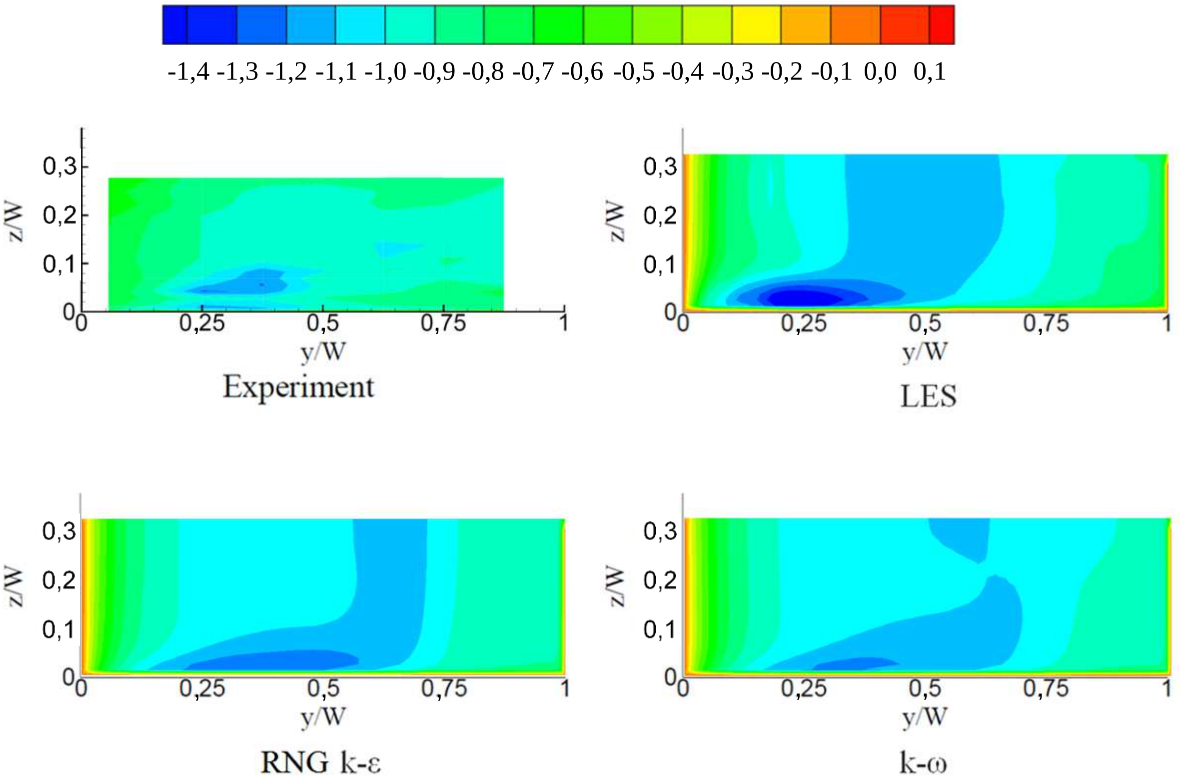

Figure 4.13: Cross-section of u* velocity distribution at x/W = -1

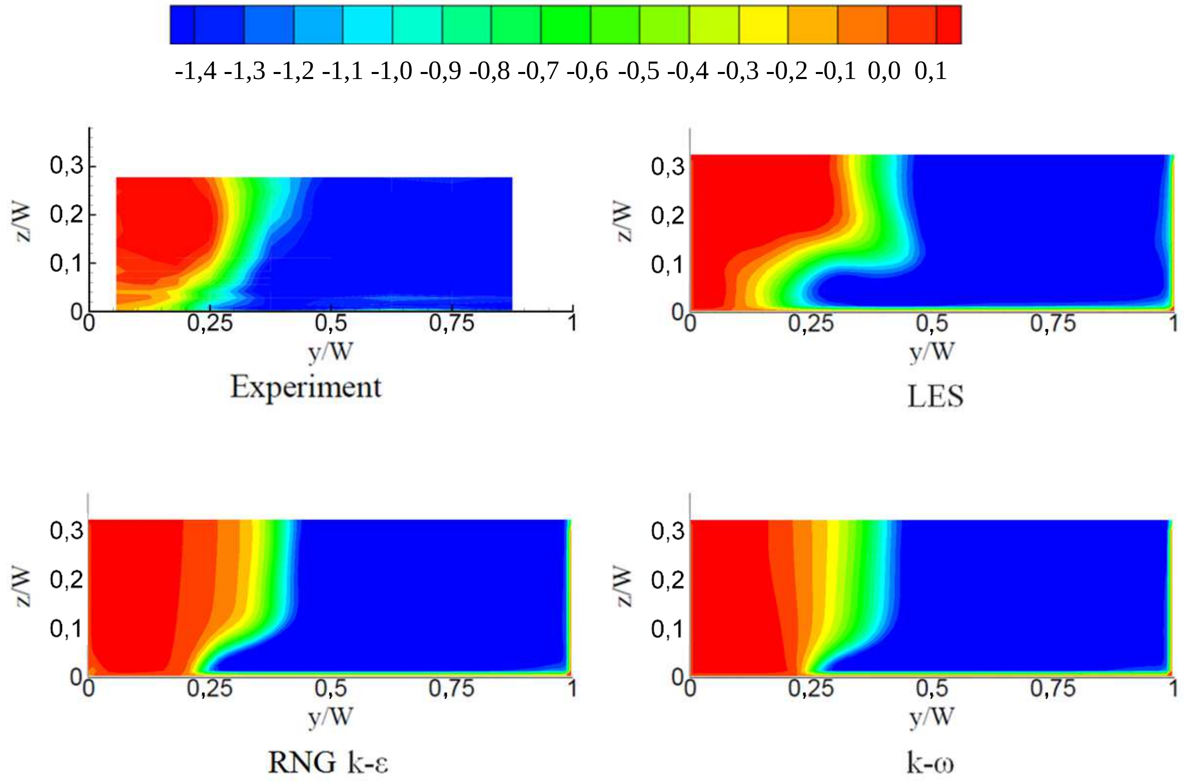

Experiment

LES

RNG k-ε

k-ω

Figure 4.14: Cross-section of u velocity distribution at x/W = -1,67

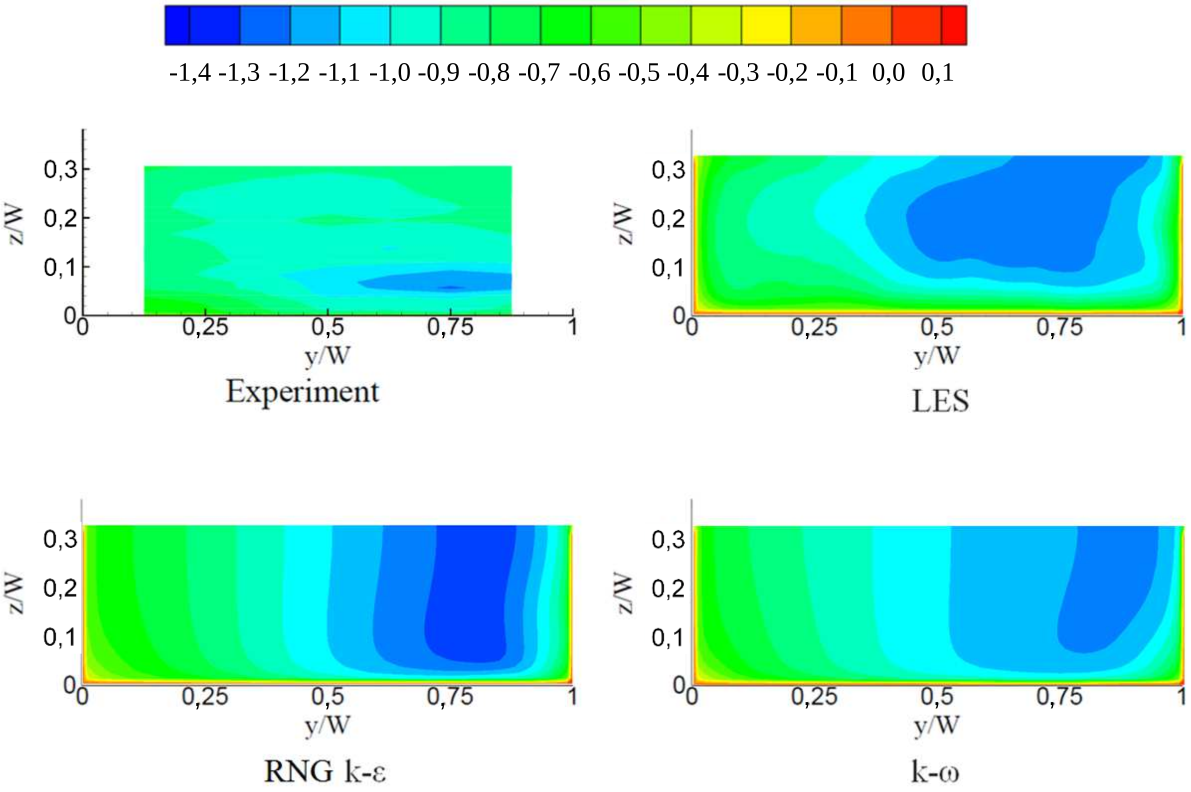

Experiment

LES

RNG k-ε

k-ω

Figure 4.15: Cross-section of u* velocity distribution at x/W = -7

4.3 Transversal velocities

In this section, only vertical profiles will be used to present the results of transversal velocities (Figure 4.16 to Figure 4.19). Velocity component v is defined in the y direction, which is positive pointing to the right-wall of the main channel (looking downstream).

Different from section 4.2.1, in this section profiles at cross-sections in the upstream channels (x/W = 1 and y/W = -1) are not presented, since the figures where the experimental results were collected from Huang (2000) do not present a good scale. Anyway, the magnitude of these velocities is not significant to be evaluated.

At cross-section x/W = 0 (Figure 4.16), though the transversal velocities are small, it is noted that the main channel flow at the upstream reach already starts being conducted to the right side of the main channel, due to the approximation to the side channel. A good accuracy was achieved by the numerical models, especially by the LES model.

Figure 4.17 shows the transversal velocities at x/W = -1, which are very large due to the entrance of the side channel flow. The numerical models did not behave well, especially at the right-sided profile (y/W = 0,75), where it is detected that the reflection of the lateral flow against the right-wall is already present, as the velocities at the bottom start pointing to the left (negative values). The model of Huang *et al.* (2002) also do not capture this negative values.

At x/W = -2 (Figure 4.18), the agreement was good in the left and middle profiles, especially by the k-ω model. However, near the right-wall (y/W = 0,75), the models could not replicate the intensity of the reflection from the right-wall, which is stronger at this section. This weakness of not being able to properly reproduce the reflection is also present in the k-ε model of Huang *et al.* (2002), as revealed in Figure 2.14.

Lastly, by evaluating Figure 4.19, it can be realized that at x/W = -6 the secondary current had most of its energy dissipated, since now the transverse velocities have much smaller magnitudes. Nevertheless, it is evident that a big helicoidal current of small velocities was actually formed upstream and it is still present at this reach, as the velocities at the bottom flow to the left and at the surface to the right. Such pattern is a consequence of the reflection at the right-wall and, as already mentioned, the models were not precise in this flow pattern.

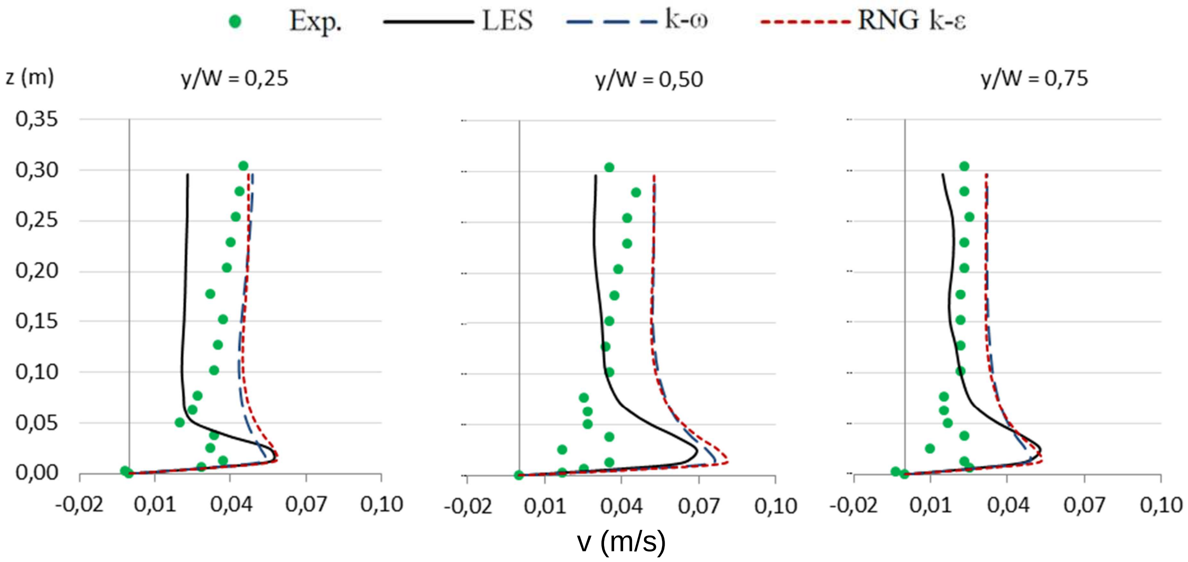

Figure 4.16: Vertical profile of transversal velocities at x/W = 0

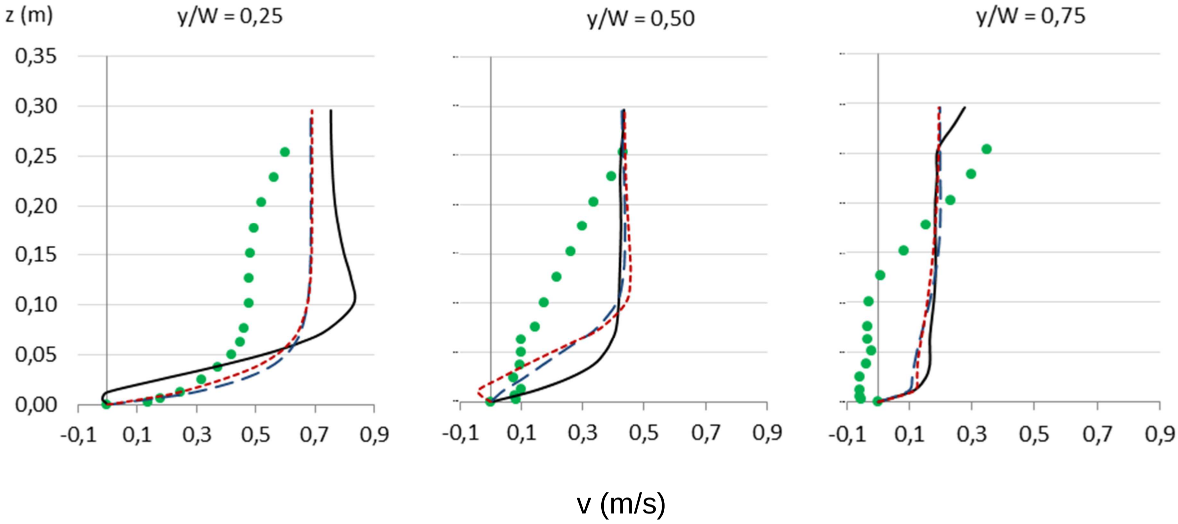

Figure 4.17: Vertical profile of transversal velocities at x/W = -1

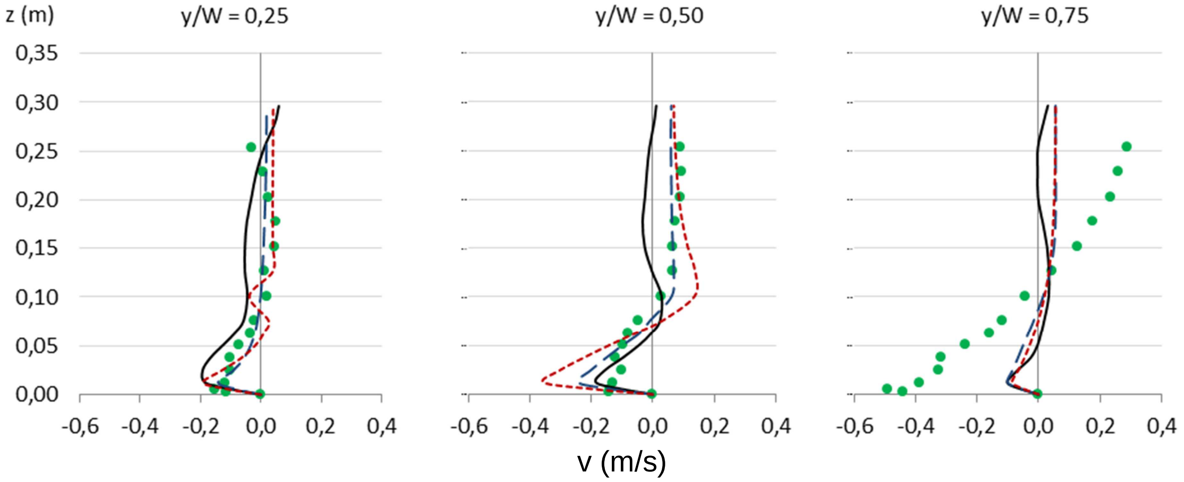

Figure 4.18: Vertical profile of transversal velocities at x/W = -2

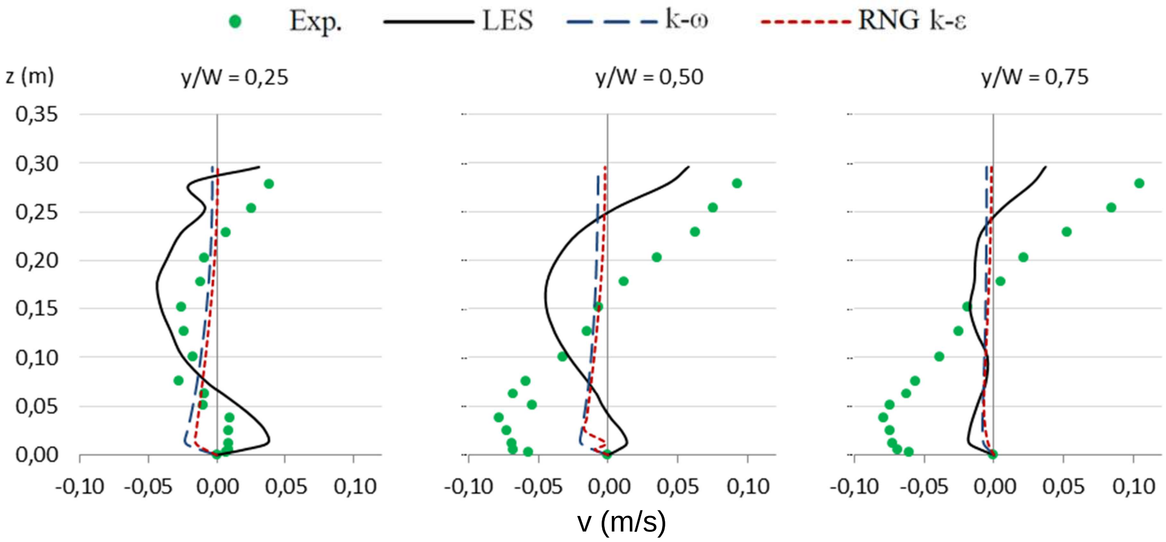

Figure 4.19: Vertical profile of transversal velocities at x/W = -6

5 CONCLUSIONS

The fluid dynamics in a confluence is not simple. Some of its challenging flow patterns to be modeled are: the formation of a separation zone in the main channel left wall downstream the junction; the appearance of a point of stagnation in the confluence upstream corner; the shock and deflection of the side channel flow against the main channel right-wall; the magnitude of the longitudinal velocities in the contracted region in the right side of the main channel; and the clockwise helicoidal current created along the downstream channel.

In this research, a three-dimensional numerical model of a 90° open channel confluence was set up and three cases applying different turbulence models were evaluated for q* = 0,250. By comparing the velocity fields simulated by numerical models to those available in the experimental data, it can be concluded that most of the flow characteristics in this confluence was captured and, therefore, the main goal of this research was achieved.

Though the general flow behavior generated by the numerical models was in good agreement with the experimental results, some limitations were found:

- The rigid lid approach caused a small but negative impact on the velocity magnitudes [in accordance with Dordevic (2012)] – especially at the inlets, where the water level difference is about 10%, what possibly diminishes the accuracy of the models along the structure.
- Moreover, none of the turbulence models could reproduce properly the secondary current or the reflection of the branch channel flow against the right-wall and its consequent helicoidal current downstream the junction, what also happened in the model of Huang *et al.* (2002).
- Looking at the main channel inlet, it can be observed that the LES model really underpredicts the velocities near the bottom and, consequently, overpredicts those near the water-surface. This is in agreements with the findings of Ramamurthy *et al.* (2013).

The comparison of the turbulence models accuracy was made throughout the discussion. Since this comparison was long and usually qualitative, it is not easy to conclude which turbulence model was the most effective. However, some aspects were clear:

- Though the LES model was meant to be very powerful to reproduce eddies and secondary currents, and in fact it showed a capacity of capturing some unique details of the flow current, at most locations its accuracy in terms of magnitude was worse than the two-equation turbulence models'. Quantitatively it was found that its separation zone was 20% shorter and more than 20% wider than in the physical model. It is also clear that the LES model underestimated the velocities closer to the walls and bottom, what might influence negatively the flow prediction as a whole.
- No big differences could be found between the RNG k-ε and the k-ω models. Their velocity magnitudes were very similar. The separation zone, though, was better predicted by the RNG k-ε model. Since this is the main concern when designing a confluence, it can be said that the RNG k-ε was the most accurate model.

Other remarks can be extracted when the numerical models developed here are compared to those available in literature that modeled the same geometry:

- The rigid lid approach did not affect the reproduction of the main flow features in the confluence. Except for the difference in velocity magnitudes at inlets, no other important feature was significantly affected by this simplification, since basically the same quality of results were found by Huang *et al.* (2002), who applied the k-ε turbulence model and tried to capture the free-surface by a sort of mesh-regeneration method. Actually, at some critical locations, such as the recirculation zone, the two-equation turbulence models developed here performed even better than Huang's model.
- Though the focus of this research was to discuss the impact of applying different turbulence models and different surface treatment methods, the accuracy of a numerical model indeed does not depend only on these two variables, but on a range of modeling settings and numerical methods to be adopted. This conclusion is based on the fact that the results obtained by Dordevic (2012) are satisfactory but significantly worse than the results from the RNG k-ε model developed here. The same author also adopted a rigid lid and applied the standard k-ε turbulence model (as robust as the RNG k-ε) for q* = 0,583, which is a flow scenario less difficult to reproduce than q* = 0,250.

OpenFOAM was crucial for the development of this work. It could be seen along the research that the software has a wide range of tools that, if accessed appropriately, can be very useful to simulating different flow cases. Nevertheless, the lack of interface in the pre-processing phase and the lack of in-depth material about the program tools might stop the user from building his model quickly and correctly.

For future studies it is recommended the development of new numerical models of confluences that perform Large Eddy Simulations as well, in order to confirm if LES turbulence models are really not suitable for reproducing the flow patterns of a confluence, or to deny the suspicious findings of this research regarding the bad accuracy of the LES model.

It would be also interesting if future studies could develop similar works that apply solvers to simulate multiphase flows. Though the rigid lid (single fluid) approach could be used in this study case without significant damage, since the water level difference was small along the structure, in nature or in most hydraulic structures the big water level variation does not allow the rigid lid approach to be used. The simple provision of detailed settings of a successful multiphase subcritical flow on a hydraulic structure would be of great contribution to the field of CFD modeling and would enhance the attractiveness of OpenFOAM for the design of hydraulic structures.

REFERENCES

Biron, P., Best, J. & Roy, A., 1996. Effects of bed discordance on flow dynamics at open channel confluences. *Journal of Hydraulic Engineering*, 122(12), pp.676–682.

Chai, X. & Mahesh, K., 2010. Dynamic k-equation model for large eddy simulation of compressible flows. In *40th Fluid Dynamics Conference and Exhibit*. Chicago, Illinois, 2010. American Institute of Aeronautics and Astronautics.

Dordevic, D., 2012. Application of 3D numerical models in confluence hydrodynamics modelling. In *XIX International Conference on Water Resources*. University of Illinois at Urbana-Champaign, 2012.

Frei, W., 2013. *COMSOL Blog*. [Online] Available at: http://www.comsol.com/blogs/which-turbulence-model-should-choose-cfd-application/ [Accessed 1 May 2014].

Gurram, S.K., Karki, K.S. & Hager, W.H., 1997. Subcritical junction flow. *Journal of Hydraulic Engineering*, 123(5), pp.447-55.

Huang, J., 2000. *Development and validation of a three-dimensional numerical model for application to river flow*. PhD Thesis ed. Iowa City: University of Iowa.

Huang, J., Weber, L.J. & Lai, Y.G., 2002. Three-dimensional numerical study of flows in open-channel junctions. *Journal of Hydraulic Engineering*, 128(3), pp.268-80.

Keylock, C.J., Constantinescu, G. & Hardy, R.J., 2012. The application of computational fluid dynamics to natural river channels: Eddy resolving versus mean flow approaches. *Geomorphology*, 179, pp.1-20.

Launder, B.E. & Spalding, D.B., 1974. The numerical computation of turbulent flows. *Computer Methods in Applied Mechanics and Engineering*, 3(2), pp.269-89.

Mamedov, A.S., 1989. Hydraulic calculation of a confluence. *Hydrotechnical Construction*, September. pp.553-56.

OpenFOAM, F., 2014. *User Guide*. 230th ed. Paris: ESI Group.

Ramamurthy, F.A.S., Han, S.S. & Biron, P.M., 2013. Three-dimensional simulation parameters for 90° open channel bend flows. *Journal of Computing in Civil Engineering ASCE*, 27(3), pp.282-91.

Rodi, W., Constantinescu, G. & T., S., 2013. *Large-Eddy Simulation in Hydraulics*. 1st ed. London: CRC Press, Taylor & Francis Group.

Sagaut, P., 2006. *Large Eddy Simulation for Incompressible Flow*. 3rd ed. Berlin: Springer.

Schlichting, H., 1979. *Boundary-layer Theory*. 7th ed. New York: McGraw-Hill.

Shabayek, S., Steffler, P. & Hicks, F., 2002. Dynamic model for subcritical combining flows in channel junctions. *Journal of Hydraulic Engineering*, 128(9), pp.821-28.

Taylor, E.H., 1944. Flow characteristics at rectangular open-channel junctions. *Transactions of the American Society of Civil Engineers*, 109, pp.893–902.

Thanh, M.D., Kimura, I. & Shimizu, Y., 2010. Depth-averaged 2D models with effects of secondary currents for computation of flow at a channel confluence. In *River Flow 2010.*, 2010.

Versteeg, H.K. & Malalasekera, W., 2007. *An introduction to computational fluid dynamics - the finite volume method*. 2nd ed. Essex, England: Pearson Prentice Hall.

Webber, N.B. & Greated, C.A., 1966. An investigation of flow behaviour at the junction of rectangular channels. *Proc., Instn. of Civ. Engrs., Vol. 34*, pp.321-34.

Weber, L.J., Schumate, E.D. & Mawer, N., 2001. Experiments on flow at a 90° open-channel junction. *Journal of Hydraulic Engineering*, 127(5), pp.340-50.

White, F.M., 1991. *Viscous Fluid Flow*. 2nd ed. New York: McGraw-Hill.

Wilcox, D.C., 1988. Reassessment of the scale-determining equation for advanced turbulence models. *AIAA Journal*, 26(11), pp.1299-310.

Yakhot, V., Orszag, S.A., Thangam, S., Gatski, T.B. & Speziale, C.G., 1992. Development of turbulence models for shear flows by a double expansion technique. *Physics of Fluids A,* 4(7), pp.1510-20.